J. Fluid Mech. (2007), vol. 580, pp. 31–81. © 2007 Cambridge University Press
doi:10.1017/S0022112007005046 Printed in the United Kingdom

The hydrodynamic structure of unstable cellular detonations

MATEI I. RADULESCU[1]†, GARY J. SHARPE[2],
CHUNG K. LAW[1] AND JOHN H. S. LEE[3]

[1]Princeton University, Princeton, NJ, USA
[2]School of Mechanical Engineering, University of Leeds, Leeds, UK
[3]McGill University, Canada

(Received 22 August 2005 and in revised form 17 November 2006)

The study analyses the cellular reaction zone structure of unstable methane–oxygen detonations, which are characterized by large hydrodynamic fluctuations and unreacted pockets with a fine structure. Complementary series of experiments and numerical simulations are presented, which illustrate the important role of hydrodynamic instabilities and diffusive phenomena in dictating the global reaction rate in detonations. The quantitative comparison between experiment and numerics also permits identification of the current limitations of numerical simulations in capturing these effects. Simulations are also performed for parameters corresponding to weakly unstable cellular detonations, which are used for comparison and validation. The numerical and experimental results are used to guide the formulation of a stochastic steady one-dimensional representation for such detonation waves. The numerically obtained flow fields were Favre-averaged in time and space. The resulting one-dimensional profiles for the mean values and fluctuations reveal the two important length scales, the first being associated with the chemical exothermicity and the second (the 'hydrodynamic thickness') with the slower dissipation of the hydrodynamic fluctuations, which govern the location of the average sonic surface. This second length scale is found to be much longer than that predicted by one-dimensional reaction zone calculations.

1. Introduction

Research in the past 50 years has demonstrated that most self-sustaining detonations in gaseous explosive mixtures are unstable and have a three-dimensional non-steady cellular structure (Fickett & Davis 1979). Figure 1 shows an example of the simpler two-dimensional frontal cellular structure obtained in the present study, along with an explanatory sketch. The present study attempts to provide an understanding of the dynamic evolution of such structures, both locally in terms of the fine-scale details appearing with overwhelming complexity, and globally, in a hydrodynamic average sense, in order to permit a large-scale modelling of such structures. The large-scale 'cellular' dynamics are now relatively well understood. The two-dimensional cell boundaries shown in the sketch of figure 1 are formed by the intersection of transverse shock waves with the leading shock front. These shock interactions are

---

† Author to whom correspondence should be addressed. Present address: Mechanical Engineering, University of Ottawa, 161 Louis Pasteur, Ottawa, Ontario, K1N 6N5, Canada, matei@uottawa.ca

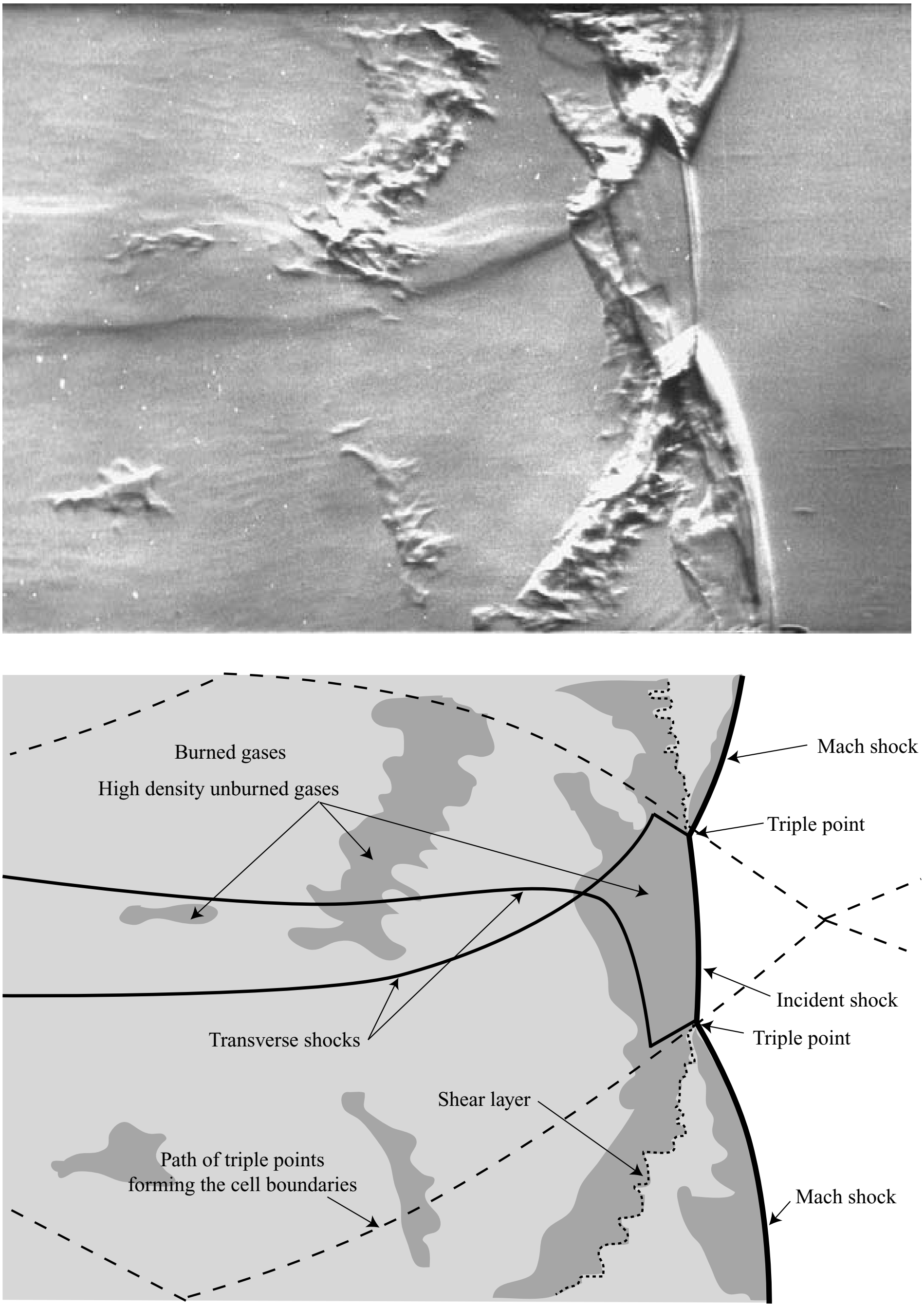

FIGURE 1. Schlieren photograph of detonation structure in a $CH_4 + 2O_2$ mixture at 3.4 kPa initial pressure in a 25 mm by 100 mm cross-section channel, and explanatory sketch.

triple-shock Mach intersections. Shear layers and transverse shocks extend from the cell boundaries into the reaction zone behind the leading shocks. The transverse shocks sweep laterally across the leading shock surface and collide with each other. They also interact and sometimes couple with the reaction layers, as can be seen near the centre of the picture in figure 1. These shock reflections also cause the leading shock front to pulsate in the direction of propagation and alternate between strong Mach stems and weaker incident shocks. Previous measurements indicate that the velocity of the leading shock generally fluctuates from approximately 0.7 to 1.6 times the average velocity between transverse wave collisions (Fickett & Davis 1979). Owing to this very large variation in leading shock strengths, the distribution of reaction rates behind the different portions of the shock can vary by up to seven orders, owing to the exponential dependence of chemical kinetic rates on temperature. This extreme shock sensitivity has been correlated with the experimental observation of unreacted pockets behind the front (Subbotin 1975; Radulescu 2003; Austin 2003; Austin, Pintgen & Shepherd 2005), which can be clearly identified in figure 1, and with the increase in irregularity of the cell structure and appearance of fine cellular sub-structure (Manzhalei 1977). These unreacted pockets have been observed in the past both computationally and experimentally with varying clarity (e.g. Edwards, Jones & Price 1970; Subbotin 1975*a*, *b*; Oran *et al.* 1982; Bourlioux & Majda 1992; Oran *et al.* 1998; Gamezo, Desbordes & Oran 1999; Sharpe 2001; Deiterding 2003; Radulescu *et al.* 2005; Austin *et al.* 2005; Inaba, Matsuo & Tanaka 2005; Hu *et al.* 2005; Eto, Tsuboi & Hayashi 2005; Deledicque & Papalexandris 2006). To date, the burning mechanism of these unreacted pockets and how it affects the detonation dynamics on the larger scales is still not well understood. Nevertheless, experiments on detonation limits suggest that the detonability of a mixture characterized by these fine-scale pockets is enhanced with respect to predictions based on the idealized one-dimensional ZND model (Fickett & Davis 1979), possibly by removing part of the thermal character of the ignition process and its sensitivity to the leading shock strength (Radulescu & Lee 2002; Radulescu *et al.* 2005).

In spite of the fact that detonation waves are three-dimensional and highly transient, experiments suggest that they propagate, on average, at a velocity within $\sim$1–2% of the value given by the one-dimensional Chapman–Jouguet (CJ) theory (Fickett & Davis 1979). This observation pre-supposes that most of the energy of the unreacted pockets is available to the detonation front and a hydrodynamic description is worthwhile. It has been proposed that the CJ theory may be valid in 'a one-dimensional transverse-average sense' (Fickett & Davis 1979), although a meaningful averaged treatment of the highly unsteady three-dimensional detonation wave structure is still lacking. Furthermore, the CJ theory rests on the hypothesis that the burned gases are in chemical equilibrium and the flow of the products is sonic relative to the front. It is thus of interest to determine if the rear of a real three-dimensional unsteady detonation can be described, at least in an average sense, by the equilibrium values derived from CJ theory and by an average rear sonic surface. This would serve as a limiting characteristic surface propagating at $u* + c*$ (see figure 2), which has to equal the detonation wave velocity V and separates the statistically averaged detonation structure from any trailing unsteady expansion waves (Taylor 1950). We note that the dynamics of the instantaneous limiting characteristic surface, as it varies with time, was recently studied numerically by Kasimov & Stewart (2004) for one-dimensional pulsating detonation waves. For a turbulent multi-dimensional detonation this would be much more difficult. Instead, we are interested in its mean location, situated at some distance behind the mean detonation front, which henceforth defines the hydrodynamic thickness.

We are hence interested in determining the average reaction zone structure of detonations. This serves as the basis for the construction of a stochastic one-dimensional model for detonations. Such a model would be highly desirable in view of the

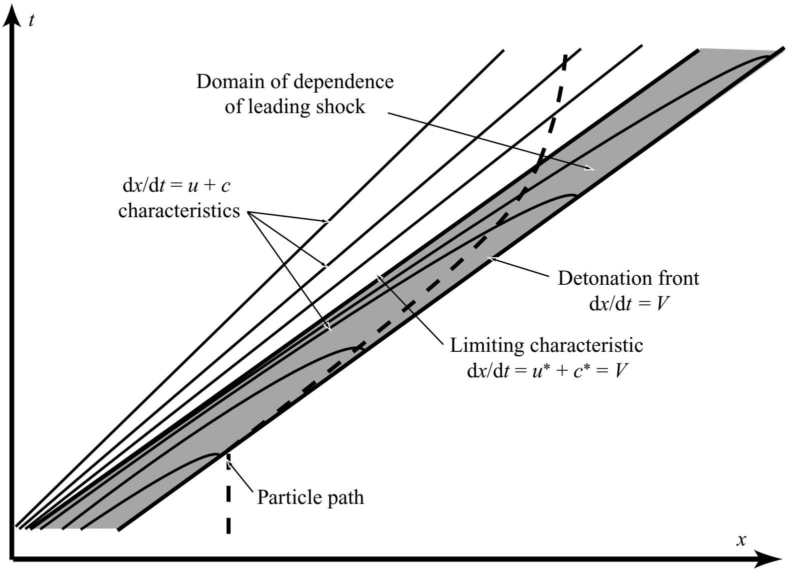

Figure 2. $x - t$ diagram illustrating the limiting characteristic at the sonic locus in the detonation frame of reference.

stochastic properties of sufficiently unstable detonations. For example, Ng *et al.* (2005*a*, *b*) and later Henrick, Aslam & Powers (2006) showed that the nonlinear dynamics of one-dimensional unsteady detonation waves follows the classical route to chaos via period-doubling bifurcations governed by the Feigenbaum constant and the appearance of odd periods. Based on their study, parameters characterizing most gaseous detonation waves would fall in the fully chaotic regime. A stochastic one-dimensional treatment of detonation waves and the consequence of fluctuations on the nature and location of the sonic surface has been attempted in the past in a number of studies (Voitsekhovskii, Mitrofanov & Topchian 1963; White 1961; Strehlow 1971; Panton 1971; Rybanin 1966; Nikolaev & Zak 1989; Lee & Radulescu 2005), where the governing equations of motion were Reynolds averaged, and their qualitative properties compared to the CJ theory for laminar flow. Two main relaxation processes were identified, one associated with the chemical exothermicity, and the second with the generation and dissipation of mechanical and thermal fluctuations in the reaction zone, which can act as both a sink and source of energy in the mean flow. Although these processes were not quantified, it was argued that detonations could be of the eigenvalue type with deviations from the ideal CJ theory depending on the magnitude of fluctuations and their rates of dissipation. A consequence of the model is that the location of the sonic surface can be associated with the competition of the various relaxation rates, in the same spirit as the action of loss terms such mass divergence, heat loss or frictional forces (Fickett & Davis 1979). Unfortunately, experiments could not clearly substantiate the above phenomenology, due to limitations in obtaining sufficiently accurate experimental measurements (see Fickett & Davis 1979 for an extensive review of available experiments to that date).

One noteworthy study however is that of Edwards, Jones & Phillips (1976), who attempted to identify the location of the sonic surface in real detonations from pressure data measured along the detonation tube wall. They measured the location of the onset of the expansion wave, which was approximately 4λ to 10λ downstream of the leading front, where λ is the preferred spacing between interacting detonation modes or 'cell size'. The onset of the expansion wave also corresponded to the length scale where the pressure oscillations from transverse shocks have decayed to a negligible intensity. They interpreted their results for the delay of the sonic surface as due to the slower dissipation of the turbulent energy. Edwards *et al.*'s estimates for the location agreed well with the earlier measurements of Soloukhin for the onset of the Taylor expansion, whose results also indicate that the onset of the expansion wave is situated approximately 4λ downstream of the leading front (Soloukhin 1966).

In the present study, we investigate the validity of a hydrodynamic description of detonations by combining complementary numerical simulations and experiments on the structure. Our focus is to determine the physical processes governing the global length scale (or time scale) of chemical energy addition at the front and the length scale for the subsequent decay of fluctuations. We investigate these processes in a hydrodynamic average sense, where we seek the statistically steady structure of unstable cellular detonations by space and time averaging. The present study improves upon a previous attempt by Gamezo *et al.* (1999). The averaging procedure used by Gamezo *et al.* (1999) appears inadequate because changes in density were not taken into account when computing the averages, which were obtained simply by arithmetic means of the various properties. The significance of the mean variables obtained in such an averaging procedure is very complicated due to higher-order terms appearing when the governing equations are formally averaged by their procedure (Favre 1965). For detonation waves, where we seek the average thermodynamic state history of many statistically identical fluid elements traversing the detonation front, a Favre-average procedure appears more adequate (Voitsekhovskii *et al.* 1963), where the density of each fluid element is used to normalize the average properties convected along with that fluid element (i.e. momentum and energy density).

Experiments on highly unstable methane–oxygen detonations are presented in § 2, in order to determine the structure of the wave and the global length scales governing the reactions. Section 3 presents the numerical counterpart to the experimental study, which provides the detailed temporal resolution lacking in the experiments and permits a reconstruction of the average profiles. Section 4 presents further numerical simulations of weakly unstable detonations characterized by regular cellular structures and a much weaker reaction rate dependence on fluctuations. We conclude the paper with further discussions of the stochastic modelling of detonations waves. The details of the Favre-averaged equations and their application to one-dimensional stationary flows are derived in the Appendix.

2. Experiments

A series of experimental tests was performed for visualization of highly unstable detonations in order to determine the details of the reaction zone structure and its average thickness. The experiments were performed at the Shock Wave Physics Group Laboratory at McGill University. The experimental set-up, described in Radulescu *et al.* (2005), consists of a channel of 25 mm by 100 mm cross-section. Stoichiometric methane–oxygen mixtures were prepared by the method of partial pressures and left to diffusively mix for at least 24 hours in a high-pressure vessel prior to their injection in the evacuated apparatus. The detonations were initiated approximately 1000 mm before the test section via an exploding wire delivering of the order of 100 J. In the test section, schlieren photographs were taken and the velocity of the wave was estimated with a pair of PCB pressure transducers spaced 200 mm apart. The experiments were

p_o (kPa)	λ (mm)	V_{CJ} (mm μs^{-1})	M_{CJ}	$t_{e,VN}$ (μs)	Δ_i (mm)	ν (mm^2 μs^{-1})
3.4	200	2.24	6.31	62	18	1.6×10^{-3}
6	100	2.27	6.38	31	8.9	9.2×10^{-4}
10	50	2.29	6.44	17	4.8	5.6×10^{-4}

TABLE 1. Thermo-kinetic summary of $CH_4 + 2O_2$ mixtures; p_o is the initial pressure, λ the average detonation cell size, V_{CJ} and M_{CJ} the Chapman–Jouguet detonation speed and Mach number, $t_{e,VN}$ and Δ_i the chemical induction time and distance in the steady ZND model and ν the kinematic viscosity in the burned products at the CJ state.

performed at initial pressures of 10 kPa, 6 kPa and 3.4 kPa, for which the nominal cell size λ is 50 mm, 100 mm and 200 mm respectively (Laberge, Knystautas & Lee 1993). Table 1 presents the key thermo-chemical properties of the mixtures, computed with a chemical equilibrium code (Gordon & McBride 1994) and from ZND calculations described below.

A total of 19 experiments were conducted at 10 kPa, from which we determined a wave velocity that is 2.2% below the ideal CJ velocity of 2.290 mm μs^{-1} with a standard deviation of 2.4% away from the mean. Figure 3 shows two of the schlieren photographs obtained. They illustrate well the fine-scale unreacted pockets near the front and the long tailed transverse shock waves intersecting the main front at triple points. Photograph (*a*) was taken with a horizontal schlieren knife edge, while (*b*) was taken with a vertical knife edge. The horizontal knife edge captures the density gradients perpendicular to the front, such as the transverse shocks and density gradients present in transverse reaction layers. Note that manufacturing non-homogeneities in the glass appear in the horizontal knife edge photograph (*b*), and are not present in (*a*). In (*a*) taken with a horizontal knife edge, the direction of propagation of the transverse waves is determined by the luminosity of the wave: dark waves are compression (expansion) waves propagating downward (upward) while bright waves are waves propagating in the opposite direction. The Mach stem and incident shock portions of the leading shock can be identified from the direction of propagation of the transverse shocks. The photograph was taken when three new Mach stems are being formed at the bottom, near the centre and near the top wall, although some weaker transverse shocks can also be seen. The directionality of the schlieren system also makes it possible to determine that the density inside the pockets is much higher than that of the surrounding hot expanded gases. Austin *et al.* (2005) present similar flow fields and verify that the pockets are indeed unreacted via planar-laser-induced fluorescence of the OH radical.

To guide us in the interpretation of the schlieren photographs based on the density gradient field, we have computed the steady, one-dimensional (ZND) profile of the detonation. Figure 4 shows the ideal ZND profile for an initial pressure of 10 kPa computed with a code developed by Shepherd (1986) and the reaction mechanism of Lutz *et al.* (1988). The temperature, fluid velocity, density, thermicity ϕ, pressure and a few key species concentrations are shown as a function of time; the time origin is taken at the shock discontinuity. The results illustrate well the thermally neutral induction zone, during which the radical pool grows. The induction layer terminates after an induction time $t_{e,VN}$ of approximately 17 μs with an abrupt energy deposition lasting approximately 2 μs. The corresponding induction length is obtained from the integration of the velocity profile, yielding $\Delta_i = 4.8$ mm. The narrowness of the exothermic stage, where density gradients are the largest, guides us in interpreting the

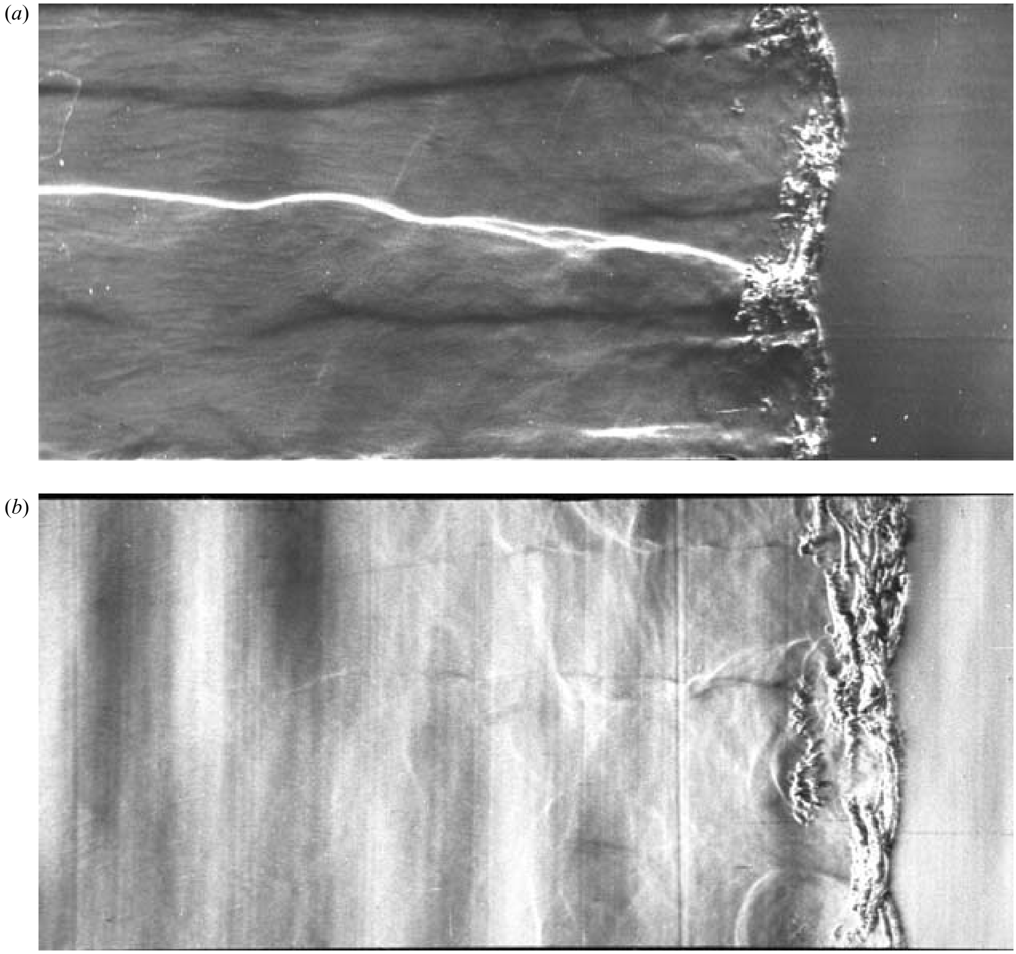

Figure 3. Schlieren photographs of the detonation structure in $CH_4 + 2O_2$ mixtures at 10 kPa initial pressure in a 100 mm by 25 mm cross-section channel; image height is 100 mm; nominal cell size is 50 mm; the horizontal schlieren cutoff (*a*) and vertical schlieren cutoff (*b*) capture respectively horizontal and vertical density gradients.

schlieren photographs, which also capture density gradients. The spotty region in the photographs can hence be associated with the high density gradients at the interface of reacted gases with gases still undergoing their induction period. The global thickness of the reaction zone can hence be easily identified in the photographs as the region where the apparent spottiness disappears. For these experiments, the global thickness of the spotty region is approximately 20 mm, meaning that shocked unreacted gas is consumed in a distance less than approximately 4 ZND induction lengths.

Very similar conclusions can be inferred from the experimental measurements of the average gas density performed by Kistiakowsky & Kydd (1956). They report X-ray absorption measurements for similar initial conditions in methane–oxygen detonations in a 10 cm diameter round tube. Their method, which integrates across the tube cross-section, showed the slow (average) density increase across the reaction zone, a clear signature of the wave three-dimensional structure and the unburned pockets (unexplainable at the time). Their measurements also showed wave thicknesses based on

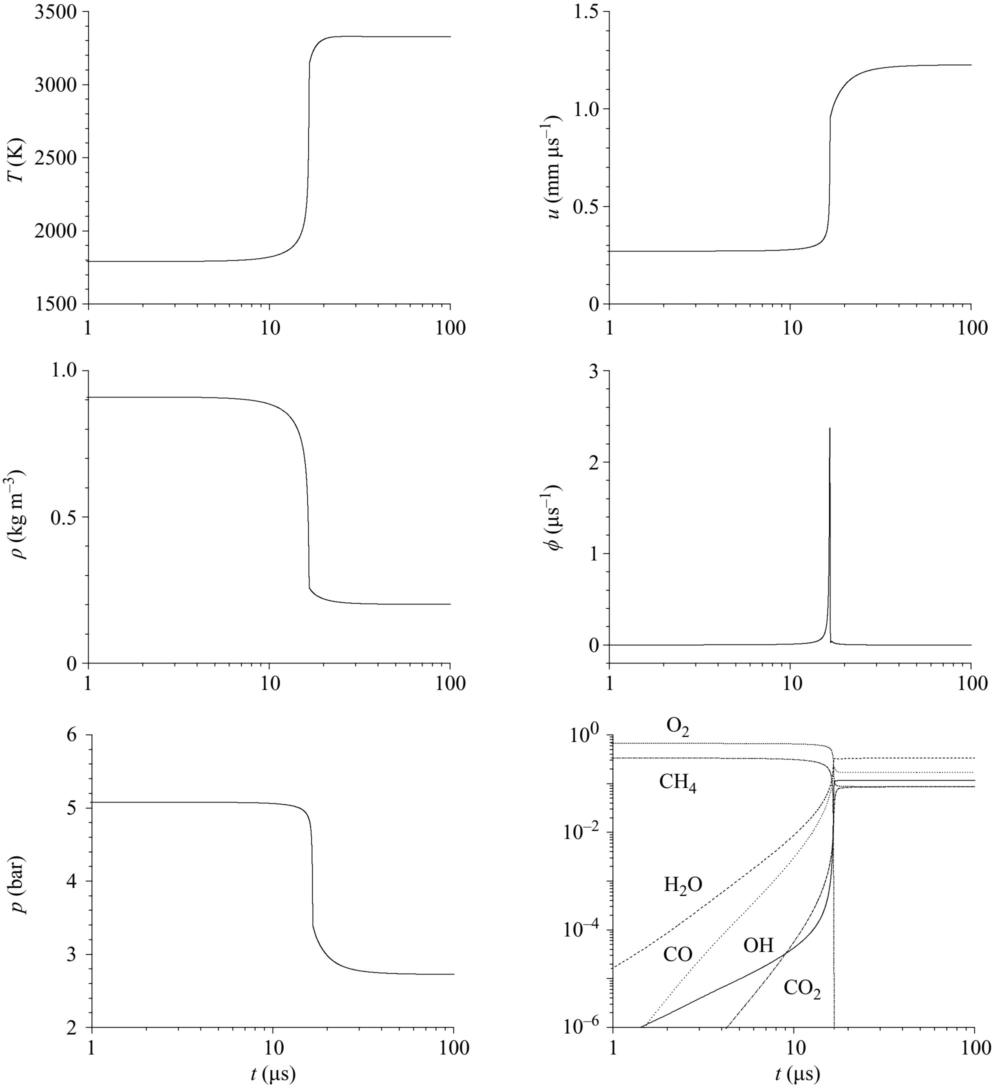

FIGURE 4. Ideal ZND detonation structure (temperature, fluid velocity, density, thermicity, pressure and key chemical species concentrations) of a $CH_4 + 2O_2$ detonation at 10 kPa initial pressure computed with the chemical kinetic mechanism of Lutz *et al.* (1988).

global density changes in the reaction zone very similar to the ones obtained in the present study.

Further experiments were performed at lower pressures of 6 kPa and 3.4 kPa, which showed that the phenomena observed scaled uniformly with the inverse of initial pressure, as expected from kinetic arguments and implied by cell size correlations. They also permitted a readier determination of the gasdynamic details of the reaction zone structure. Figure 5 shows three photographs obtained at 6 kPa initial pressure illustrating the variability observed in the flow field. Photograph (*a*) shows a mode 1 detonation with one main triple point near the top wall. The entire shock extending below the triple point is followed by the very spotty reaction zone structure. Photograph (*b*) is a mode 2 detonation where the incident shock is the central part of

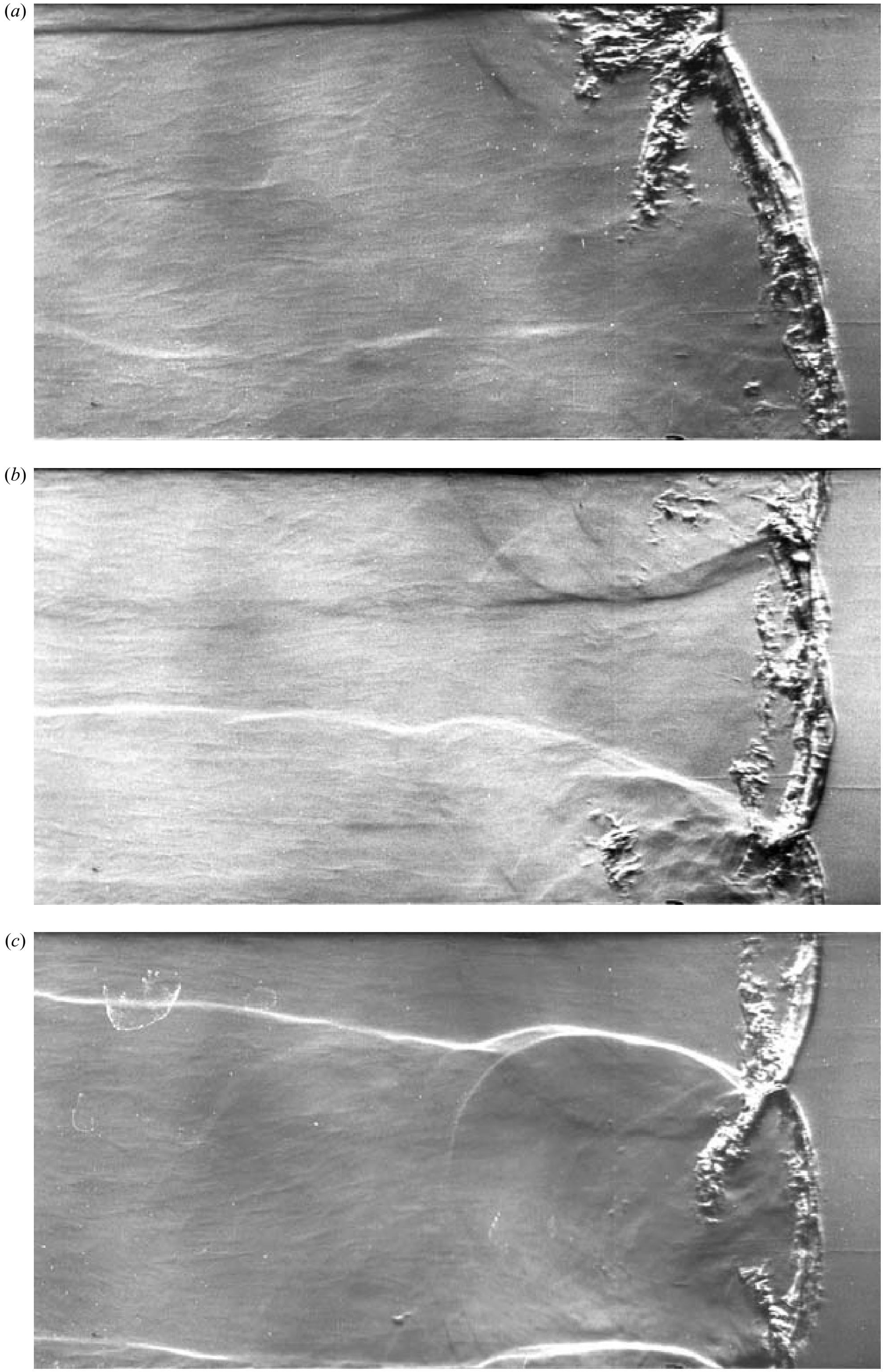

FIGURE 5. Schlieren photographs of the detonation structure in $CH_4 + 2O_2$ mixtures at 6 kPa initial pressure in a 100 mm by 25 mm cross-section channel; image height is 100 mm; nominal cell size is 100 mm.

the shock and the two triple points are propagating towards the centre of the channel, as can be deduced from the luminosity of the transverse shocks extending to the back. Perhaps the most easily understood photograph is (*c*), displaying clearly a mode 3 detonation. Two triple points are colliding near the upper part of the photograph, and a similar reflection occurs at the bottom wall. The complexity of the dynamics of the front is well-illustrated, compatible with the observations made in the past regarding cellular foils and the present results of the numerical simulations (see below). In all photographs, we also note that fine scales are always observed until the limit of the experimental technique of $\sim$1 mm, due to the motion blur from the $\sim 1\,\mu$s exposure of the photographs. Fine texture is observed behind the incident shocks and Mach stems and in the growing tongue-shaped structures engulfing the gas shocked by the weaker incident shocks.

From seven repeat experiments performed at 6 kPa, we deduced a wave velocity lower than the ideal calculated value by 2.1% with a standard deviation of 4.7%. Although wall losses may entirely account for these small velocity deficits, the fact that they are relatively small suggests that waves close to the true self-sustained fully developed detonations were established. In this sense, the sub-structure observed is not a consequence of marginality, but characteristic of these unstable detonations. The present photographs also allow the measurement of the global reaction zone thickness, yielding a total burnout of all the gases processed by the front in less than approximately 30 mm. For this initial pressure, the ZND induction length is 8.9 mm, meaning that most gases are consumed in less than $\sim$4 ZND induction lengths.

At the lower pressure of 3.4 kPa, although the cellular structures are large enough to permit detailed observation, wall losses begin to play a more significant role. From seven consecutive experiments, a velocity deficit of 20% is observed, with a standard deviation between experiments of 5.8%. Figure 6 shows two photographs, clearly illustrating the reaction zone structure of the detonation wave. The various features are indicated in the sketch of figure 1. In all photographs, the central part of the front is the weaker incident shock, observed at various stages of the cellular dynamics. Also clearly visible are the unreacted tongues of gas corresponding to gases shocked by the incident shock and transverse shocks at an earlier time. The filamentary structure of the shear layers separating burned and unburned gases can be clearly identified, which persists at the boundary of the unreacted pockets. A complete re-construction of the flow field will be given below based on the numerical simulations, which provide the large-scale temporal resolution lacking in the experiments.

Although the channel size is approximately half a nominal cell, multiple modes are observed on the structure. The dynamics of the front changes between double mode and single mode, the latter being presented in Radulescu *et al.* (2005). These photographs also allow the revision of an incorrect interpretation given by Radulescu *et al.* (2005) regarding one of their earlier photographs (Fig. 2A in their paper). The 'bulge' observed in their photograph, assumed to be associated with an explosion event in a mode 1 detonation, is in fact a consequence of the interaction of multiple modes of the frontal structure, such as those of figure 6. The error was confirmed later by Kiyanda, Higgins & Lee (2005), who repeated the experiments with multiple frame capabilities.

One such experiment conducted by Kiyanda using the same experimental set-up and initial conditions is shown in figure 7 (Kiyanda 2005). It illustrates a sequence of four consecutive frames taken at 20 µs interval of a mode 1 detonation at 3.4 kPa. Column (*a*) presents the schlieren photographs taken with a vertical knife edge, while column (*b*) shows two simultaneous self-luminescence records taken with a separate digital camera, which captures the regions of chemical reaction and to some extent

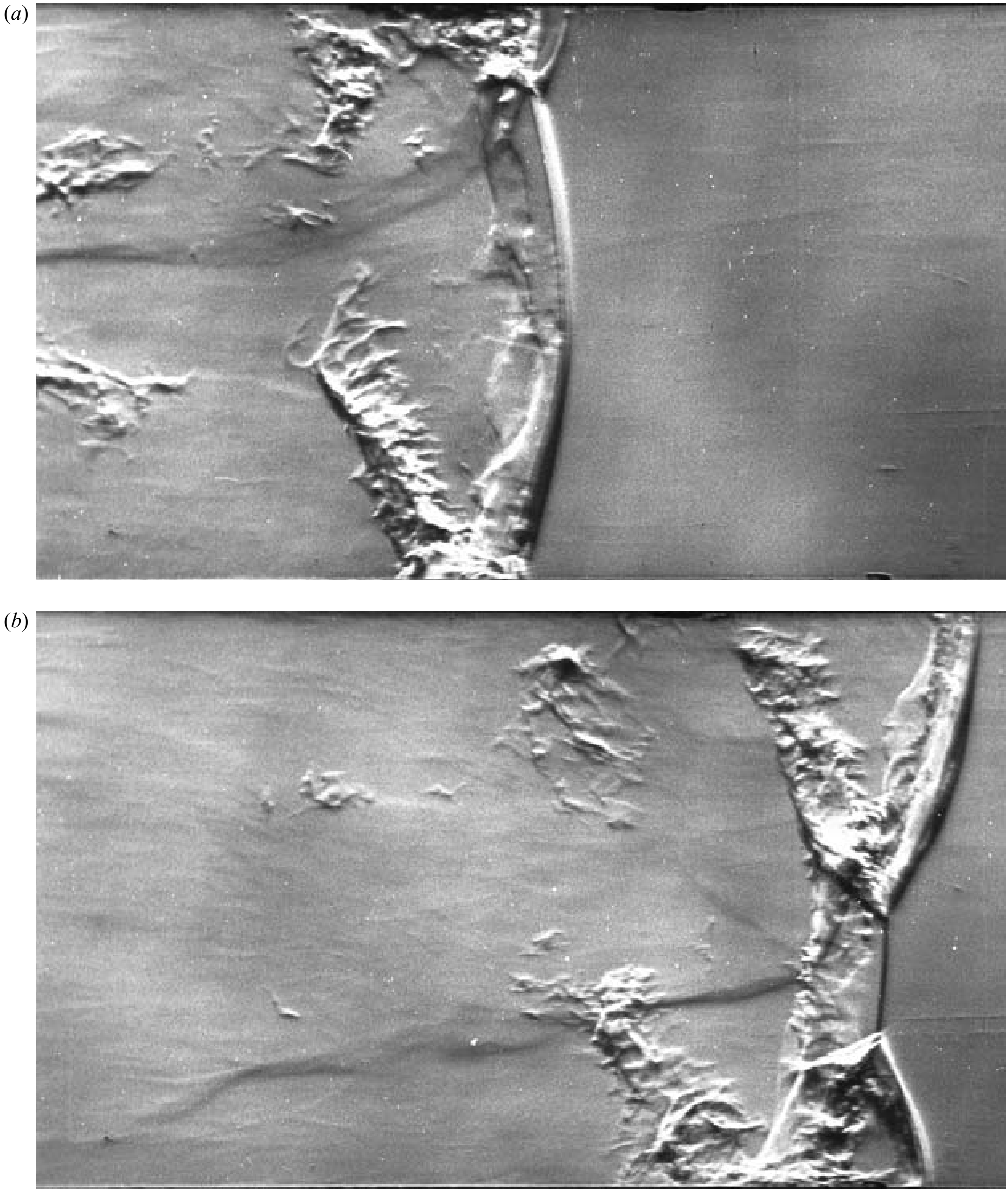

Figure 6. Schlieren photographs of the detonation structure in $CH_4 + 2O_2$ mixtures at 3.4 kPa initial pressure in a 100 mm by 25 mm cross-section channel; image height is 100 mm; nominal cell size is 200 mm.

the emission from the shocked hot gases. In the first frame, the triple point is close to the top wall and is propagating downwards. The bottom portion of the lead shock is the incident weaker shock. The sequence of photographs illustrates well the regions of intense chemical reaction behind the Mach shock and the filamentary intermittent nature of the chemical activity behind the incident shock and in the unreacted pockets.

At 3.4 kPa, both our photographs and those of Kiyanda reveal that the pockets are consumed within a distance of 100 mm behind the front. The ZND induction length Δ_i of a CJ detonation is 18 mm, implying that the pockets are consumed within less

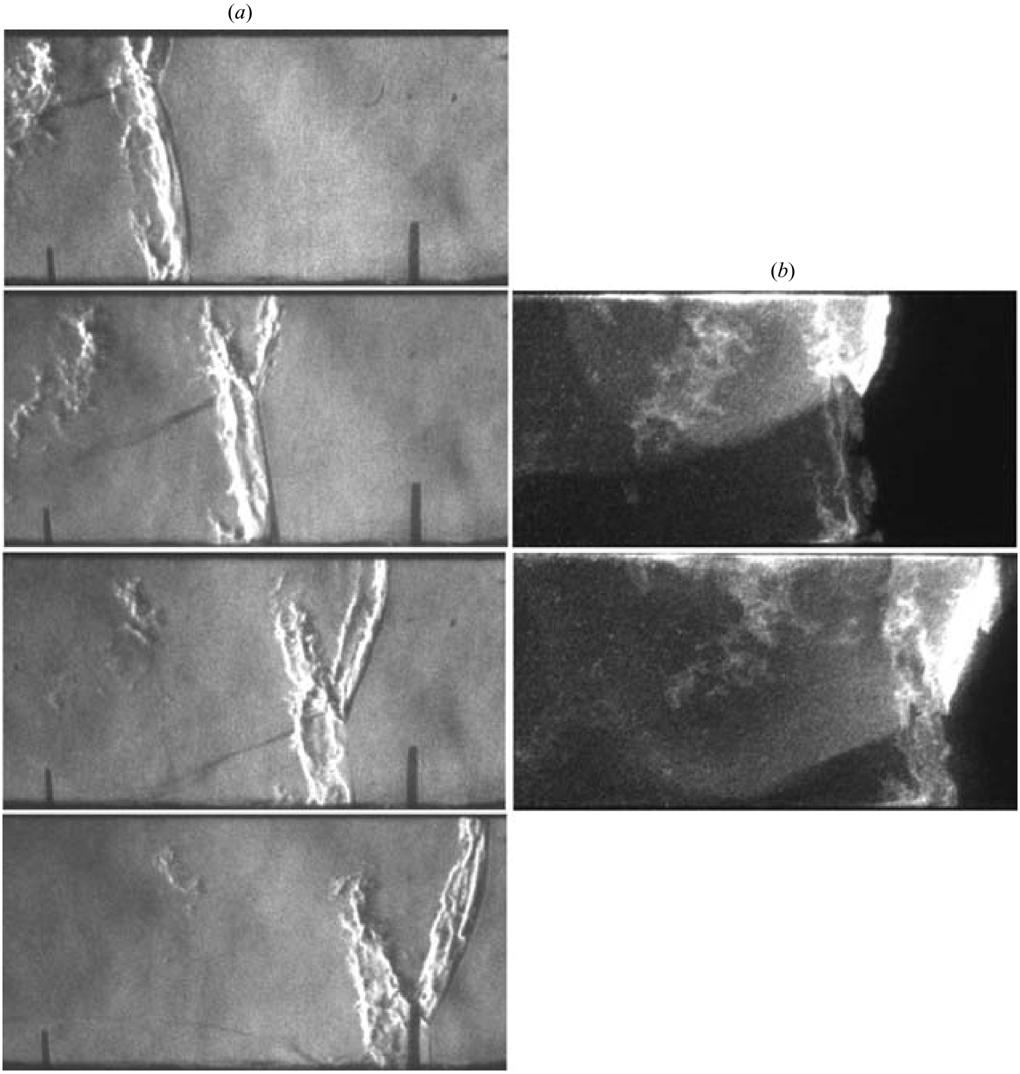

FIGURE 7. Sequence of schlieren photographs (*a*) and (*b*) self-luminosity of the detonation structure in $CH_4 + 2O_2$ mixtures at 3.4 kPa initial pressure in a 100 mm by 25 mm cross-section channel; image height is 100 mm; nominal cell size is 200 mm; frames taken at 20 µs interval (courtesy of Charles B. Kiyanda).

than $\sim 6\Delta_i$. It is remarkable that the pockets burn out within less than 100 mm, in spite of the fact that the wave propagates with a global velocity deficit of 20%. Hence, the conclusion obtained from the above experiments at all the pressures investigated is that in spite of the large fluctuations observed on the detonation structure, the global reaction zone thickness of the wave was always of the order of 4–6 ZND reaction zone lengths.

When one considers the ignition delays behind the various portions of the wave, such as at the low-velocity incident shocks propagating at $\hat{V} \approx 0.7\hat{V}_{CJ}$ (see figures 6 and 7), it is difficult to account for the observed rapid burnout of the pockets with diffusionless ignition alone as the burning mechanism. Quantitatively, the ignition delay dependence on the shock state can be modelled by a one-step Arrhenius dependence. The activation energy was obtained from the Lutz *et al.* (1988) mechanism via constant-volume homogeneous explosion simulations over the range of temperatures of interest. Normalized by the shock temperature, we obtain an activation energy of $\theta_{VN} = \hat{E}_a/\hat{R}\hat{T}_{VN} = 11$. This value is in very good agreement with the value deduced experimentally by Thomas & Edwards (1983) for methane–oxygen mixtures ignited by decaying incident shocks. Since the activation energy is sufficiently large, one can make the Frank–Kamenetskii approximation to obtain the local homogeneous explosion time $\hat{t}_e$ (Williams 1985). The ratio of $\hat{t}_e$ and the explosion time behind the shock at the von Neumann state $\hat{t}_{e,VN}$ thus becomes

$$\frac{\hat{t}_e}{\hat{t}_{e,VN}} = \left(\frac{\hat{T}}{\hat{T}_{VN}}\right)^2 \exp\left[\theta_{VN}\left(\frac{\hat{T}_{VN}}{\hat{T}} - 1\right)\right], \tag{2.1}$$

which shows the exponential dependence of the characteristic reaction times on local temperature. Since we are dealing with strong detonations with $M_{CJ}^2 \gg 1$, one can further make the strong shock approximation, for which

$$\frac{\hat{T}}{\hat{T}_{VN}} \cong \left(\frac{\hat{V}}{\hat{V}_{CJ}}\right)^2 \tag{2.2}$$

and the ignition delay can hence be written as

$$\frac{\hat{t}_e}{\hat{t}_{e,VN}} = \left(\frac{\hat{V}}{\hat{V}_{CJ}}\right)^4 \exp\left[\theta_{VN}\left(\frac{1}{(\hat{V}/\hat{V}_{CJ})^2} - 1\right)\right], \tag{2.3}$$

which shows that the ignition delay behind an incident shock with velocity $\hat{V}/\hat{V}_{CJ} = 0.7$ is lengthened by a factor 2×10^5. The great lengthening of the induction time expected for diffusionless ignition is completely inconsistent with the experimental observations, which show reaction times a few orders of magnitude shorter.

A further interesting observation relates to the ∼20% global velocity deficit in the experiments performed at 3.4 kPa. From (2.3), this velocity deficit would lead to an increase of the ignition delay time of the bulk of the gases by a factor of 200, had diffusion been negligible. One would hence expect a lengthening of the structure by two orders of magnitude. This is not the case, as the reaction zone thickness is only minimally affected by the velocity deficit: the shocked gases react within $\sim 6\Delta_i$, compared to $\sim 4\Delta_i$ for the non-marginal waves at higher pressures. This is thus indicative of how the multi-dimensional structure of the wave removes most of the thermal character of the global reaction rate, already observed in limit experiments (Radulescu & Lee 2002). We will discuss this effect in detail below when we analyse the reaction zone structure for highly unstable detonations determined numerically.

3. Simulations of methane–oxygen detonations

3.1. *Range of scales*

Before proceeding with the numerical simulations of such unstable detonations, it is worthwhile first to estimate the expected range of scales which would require resolution. The two important length scales to be considered are that over which turbulence dissipates the energy generated via hydrodynamic instabilities in the reaction zone structure, and that corresponding to the thickness of a laminar flamelet that could be established along the contact surfaces separating reacted and unreacted gas such as the pockets illustrated in the above photographs.

The first length scale, corresponding to the Kolmogorov scale for energy dissipation, can be estimated by assuming that a turbulence cascade operates between the scales at which energy is being injected and the viscous scales. Although in reality the physical processes are very complex and involve compressible turbulence such as shock and density layer interactions, one can estimate the Kolmogorov length scale based on an order-of-magnitude phenomenological picture for the energy cascade. Following Kolmogorov phenomenology and omitting numerical coefficients of order 1 (see for example Frisch 1995), if energy is injected at the scale l_1 in the form of kinetic energy, i.e. v_1^2, the cascade requires the invariance of the energy flux all the way to the viscous Kolmogorov scale l_2, where it is dissipated into heat, yielding

$$\frac{u_1^3}{l_1} \approx \frac{u_i^3}{l_i} \approx \frac{u_2^3}{l_2}, \tag{3.1}$$

where the subscript i denotes an inertial scaling range quantity. In terms of eddy-turnaround times, (3.1) can be re-written as

$$\frac{u_1^2}{t_1} \approx \frac{u_i^2}{t_i} \approx \frac{u_2^2}{t_2}, \tag{3.2}$$

At the Kolmogorov scale l_2, the local Reynolds number is close to unity such that viscous forces can damp the eddy's motion, i.e.

$$\frac{u_2 l_2}{\nu} \approx 1, \tag{3.3}$$

where ν is the kinematic viscosity. Back substituting, we obtain the well-known result expressing the ratio of length scales separating the integral scale l_1 and Kolmogorov scale l_2 in terms of the Reynolds number evaluated at the integral scale:

$$\frac{l_2}{l_1} \approx \left(\frac{u_1 l_1}{\nu}\right)^{-3/4} \approx \left(\frac{u_1^2 t_1}{\nu}\right)^{-3/4}, \tag{3.4}$$

where t_1 is an integral time scale over which the energy is deposited. For detonations, the energy is deposited over a time scale corresponding to the exothermic stage of the reactions. We can take as a reference the time scale of the exothermic region of the ZND profile, the time interval where most of the energy is released. From figure 4, for the methane–oxygen detonation at 10 kPa, energy is deposited over a time scale of 2×10^{-6} s, during which the gas velocity changes by approximately 10^3 m s^{-1} due to expansion. The kinematic viscosity was estimated in the burned products with the Gordon & McBride equilibrium code using the data given by Svehla (1995), yielding 5×10^{-4} m^2 s^{-1} (see table 1). The resulting Reynolds number is $\sim 4 \times 10^3$, yielding a range of scales $l_2/l_1 \approx 2 \times 10^{-3}$. Since the exothermic layer is typically an order of magnitude shorter than the ZND induction zone, this yields a Kolmogorov scale smaller than the ZND induction length by a factor of 10^4. This would be the required resolution to correctly capture the turbulent diffusive layers in the detonation wave structure in numerical simulations.

An equally important length scale is the thickness of a laminar flamelet that can be established between the reacted gas and unreacted gas along the shear layers and contact surfaces. This diffusive length scale l_{diff} can be expressed in terms of the thermal diffusivity κ and the characteristic time scale of chemical energy deposition t_{chem} as

$$l_{diff} \approx \sqrt{\kappa t_{chem}}. \tag{3.5}$$

Taking the example considered above at 10 kPa initial pressure with a characteristic time for energy addition of 2×10^{-6} s, and assuming that the heat and momentum diffusivities are equal, we obtain a characteristic diffusive scale of 10^{-2} mm. For these conditions, the ZND induction length is ∼5 mm, indicating that a characteristic diffusive layer associated with laminar flamelets, neglecting the effect of turbulence, is a factor of 2×10^{-3} smaller than the ZND induction length. This length scale is larger than the Kolmogorov scale by approximately one order of magnitude in this case.

The above considerations illustrate the magnitude of the diffusive scales in gas detonations, which would require resolutions exceeding 10^4 grid points per induction length to capture the true diffusive layers. Current computational capabilities cannot address such high computational costs, and typically maximum resolutions fall short by approximately two orders of magnitude. Hence, as in all previous attempts to compute highly unstable detonation solutions, the present simulations do not resolve the fine-scale turbulent dissipation nor the diffusive phenomena associated with the molecular diffusivities, but instead focus on the larger scales of the detonation structure. The simulations hence not only necessarily cut off a range of scales which would otherwise affect the flow field, but also affect the burnout rates by introducing artificial dissipation at the larger scales. The outcome of this approximation for the resulting flow-field evolution and structure is analysed below.

3.2. *Numerical details*

For simplicity, the gas model used in the hydrodynamic simulations assumes a single reaction converting the reactive gases into products. The gases are assumed to be perfect, and the product and reactant gases are assumed to have the same specific heats and molar mass. Although the governing equations are the Navier–Stokes equations (see the Appendix), as in all previous simulations we solve a discretized version of the Euler equations:

$$\hat{\rho}_t + \nabla \cdot (\hat{\rho}\hat{\boldsymbol{u}}) = 0, \tag{3.6}$$

$$(\hat{\rho}\hat{\boldsymbol{u}})_t + \nabla \cdot (\hat{\rho}\hat{\boldsymbol{u}}\hat{\boldsymbol{u}}) + \nabla_p = 0, \tag{3.7}$$

$$(\hat{\rho}\hat{e})_t + \nabla \cdot ((\hat{\rho}\hat{e} + \hat{p})\hat{\boldsymbol{u}}) = 0, \tag{3.8}$$

$$(\hat{\rho}\alpha)_t + \nabla \cdot (\hat{\rho}\hat{\boldsymbol{u}}\alpha) = \hat{\rho}\hat{w}, \tag{3.9}$$

where the hyperbolic fluxes are augmented by artificial diffusive fluxes, as described below. The total energy $\hat{e}$ (internal, kinetic and chemical) is given by

$$\hat{e} \equiv \frac{\hat{p}/\hat{\rho}}{\gamma - 1} + \frac{1}{2}\hat{u}_i\hat{u}_i + \alpha\hat{Q}, \tag{3.10}$$

where $\hat{Q}$ is the chemical energy, α is the reaction progress variable, taken as the mass fraction of the reactant and the ‘hat’ henceforth denotes a dimensional variable. The variable notation follows the usual convention. For simplicity, we further assume that the reactions proceed via a single irreversible step given by Arrhenius kinetics:

$$\hat{w} = -\hat{k}\alpha \exp\left(-\frac{\hat{E}_a}{\hat{R}\hat{T}}\right), \tag{3.11}$$

where $\hat{E}_a$ is the activation energy and $\hat{k}$ a pre-exponential constant set through appropriate non-dimensionalization. Non-dimensionalization of the governing equations uses the half-reaction length of the steady ZND model $\hat{\varDelta}_{1/2}$ as reference scale, the ideal detonation velocity $\hat{V}_{CJ}$ as reference velocity and initial density in the quiescent gas $\hat{\rho}_o$as density scale. This sets unity time as the time required for the wave to travel one half-reaction length. Note that for large activation energies, the reaction zone structure approaches the square-wave profile of figure 4 and the half-reaction length is approximately equal to the induction length. To ease comparison with previous studies, our non-dimensional activation energy E_a and heat release Q can be written in terms of the usual scaled variables $\theta = (\hat{E}_a/\hat{R}\hat{T})$ and $\beta = (\hat{Q}/\hat{R}\hat{T})$with the following relations:

$$E_a \equiv \frac{\hat{E}_a}{\hat{V}_{CJ}^2} = \frac{\theta}{\gamma M_{CJ}^2}, \quad Q \equiv \frac{\hat{Q}}{\hat{V}_{CJ}^2} = \frac{\beta}{\gamma M_{CJ}^2} = \frac{\left(1 - M_{CJ}^{-2}\right)^2}{2(\gamma^2 - 1)}, \tag{3.12}$$

where M_{CJ} is the detonation Mach number and its relation to the heat release in (3.12) is given by Chapman–Jouguet theory (Fickett & Davis 1979).

The computation was performed in two dimensions using the μCobra code, described in Falle & Giddings (1993) and Falle (1991). It is a second-order-accurate Godunov-type scheme in which the second-order Riemann problems are constructed from the primitive variables using a quadratic averaging function. An exact Riemann solver is used wherever necessary and a linear solver elsewhere.

The code uses a hierarchical series of Cartesian grids $G^0, \ldots, G^N$, so that grid G^n has mesh spacing $h/2^n$, where h is the mesh spacing on the base grid G^0. Grids G^0 and G^1 cover the entire domain, but the higher grids only occupy regions where increased resolution is required. Refinement is controlled by comparing the solution of each conserved variable and also their rates of change on grids G^n and G^{n-1}. If either of these errors is greater than given tolerances then the grid is refined to level G^{n+1}, $n + 1 \leqslant N$. These conditions can be used to ensure that regions where the flow is changing rapidly, e.g. shocks, are always resolved to the highest level. Supplemental criteria are used to ensure that maximum resolution is used in regions of unburned gas undergoing long induction zones, where the reaction rate is very low (Sharpe 2001). In this paper, we use a base grid with a spacing of 1 point per half-reaction length and 4 to 6 refinement levels, giving effective resolutions of 32, 64 and 128 points per half-reaction length. The present code was used successfully for detonation simulations in Sharpe (2001).

In the numerical scheme, artificial diffusion was added to the momentum and energy fluxes determined from the Riemann solution in order to suppress the Quirk instability (Quirk 1992) and to remove the entropy oscillations behind slowly moving shocks, as described in Falle & Komissarov (1996). The viscous stress is defined in terms of the left and right states in the Riemann problem and the local sound speed:

$$\tau^{ij} = 0.2\rho\sqrt{p/\rho}\left(\phi_L^i - \phi_R^i\right), \tag{3.13}$$

where ϕ_L^i and ϕ_R^i are the re-constructed primitive variables (velocity u and temperature T in the momentum and energy conservation respectively) at the cell interface in the Riemann problem of the j-direction. Falle & Komissarov (1996) show that in smooth regions, where the solver is second-order accurate, the resulting diffusivities become proportional to the square of the grid spacing Δx. The highest numerical diffusivities, however, occur in regions of the flow where discontinuities are present, where the scheme becomes first order. The resulting kinematic viscosity and heat diffusivity become proportional to the grid spacing Δx (Falle & Komissarov 1996), given by

$$\kappa = \nu = 0.2\sqrt{p/\rho}\Delta x. \tag{3.14}$$

Case	θ_{VN}	β_{VN}	γ	Domain	Resolution
A	11	7.5	1.24	6×1000	128 pts/$\Delta_{1/2}$
B	11	7.5	1.24	12×1000	64 pts/$\Delta_{1/2}$
C	5.6	10.4	1.2	10×1000	32 pts/$\Delta_{1/2}$
D	5.6	10.4	1.2	10×2000	64 pts/$\Delta_{1/2}$

TABLE 2. Summary of the parameters used in the simulations.

For reference, it is useful to compare the diffusivities given by (3.14) with the real molecular diffusion coefficients. The reciprocal of the diffusivities in (3.14) is simply the Reynolds number defined in terms of the reference scales used in the non-dimensionalization, i.e. $\hat{V}_{CJ}$ and $\hat{\Delta}_{1/2}$. So for example, at the maximum resolution of 128 points, assuming a sound speed of order unity in the products, the numerical Reynolds number is $\sim 5 \times 10^3$, compared with a Reynolds number computed with the same characteristic scales for the 10 kPa methane–oxygen experiments of $\sim 2 \times 10^5$ (see table 1). This illustrates that the diffusivities in the numerical simulations are larger than in the experiments by at least two orders of magnitude. All Euler schemes will have inherent artificial diffusion with large disparities between the numerical diffusion and real diffusion at such resolutions, as was also estimated in the previous section based on length scale estimates of real diffusive phenomena and current resolutions used in simulations.

The thermo-chemical parameters were chosen to represent methane–oxygen detonations (Radulescu *et al.* 2005), corresponding to the experiments shown above. The effective activation energy, heat release and isentropic exponent are taken as $\theta_{VN} = 11$, $\beta_{VN} = 7.5$ and $\gamma = 1.24$, corresponding to $\theta_o = 63.7$ and $\beta_o = 43$; where the subscripts "o" and "*VN*" refer to the initial state and the von Neumann shock state of the ZND model, respectively. The computational domain extended to the back wall where the detonation was initiated. We hence solved explicitly the entire computational domain including the unsteady Taylor expansion wave developing behind the detonation front. The length of the computational domain was set to 1000 and the width was set to permit a 2-mode detonation (equivalent to the 6 kPa experiments above). This corresponded to setting the height of the two-dimensional channel to 12, with a maximum resolution of 64 points per half-reaction length. A narrower domain width of 6 was also used at a higher resolution of 128. We will denote these two cases as case A and case B (see table 2). Typical run times for a simulation on a personal computer at the highest resolution was of the order of a few months, although the averaging procedure required a re-run of the solution with the average detonation velocity computed in the first run. The detonation was initiated with a high-pressure region of width 1, pressure 50 and density 1 placed at the origin of the domain. A one-dimensional simulation was run for the early part of the detonation decay from the highly overdriven state until it reached $x = 120$. These one-dimensional profiles obtained were used as initial conditions for the two-dimensional simulations. A sinusoidal perturbation was then added to rapidly establish the cellular instability.

3.3. *Global features*

Figure 8 illustrates the cellular structure of the detonation wave obtained for cases A and B, obtained by recording the integrated heat release rate over time at each fixed point of the computational domain. The highest heat release rate occurs near triple

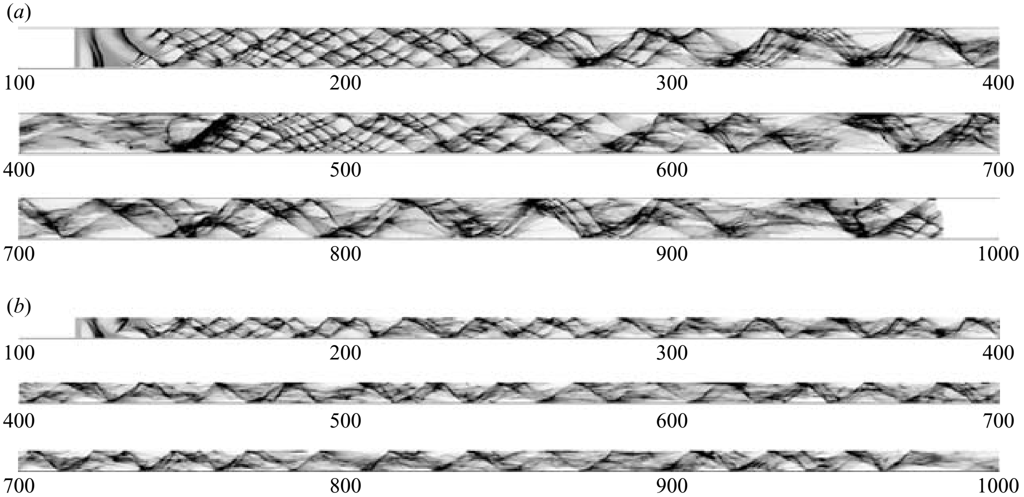

FIGURE 8. Time-integrated exothermicity illustrating the cellular structure for $\theta_o = 63.7$ detonations: (a) case A, and (b) case B.

points and hence this acts as a diagnostic for recording the tracks; see Sharpe & Falle (2000) and Sharpe (2001) for further details. The method is analogous to the 'open shutter' photographs obtained experimentally by the time-integrated luminosity technique (e.g. Radulescu & Lee 2002). For both cases, the initial perturbation gives rise to a fine cellular structure. Initially, while the wave is still overdriven, small cells appear, which then grow as the wave becomes self-sustained. In the wider domain of case A, the cellular structure is very irregular, with many modes interacting nonlinearly. The detonation appears to change its propagation mode between a mode 1, a mode 2, and a complex long-wavelength failure and re-initiation mode with intermittent bursts of new cells formed during regions of apparent disappearance of the main detonation structure. As discussed in Radulescu *et al.* (2005), these intermittent events may even quench the detonation altogether in narrower domains. This was the case for a domain width of $y = 6$ in the 64 points resolution case, presented in Radulescu *et al.* (2005). At higher resolution in the $y = 6$ domain width (case B), the detonation propagates with a preferred mode 1 structure and a significant amount of substructure.

Figures 9 and 10 show the evolution of the flow field for cases A and B during the time interval in which a detonation propagates a distance of approximately 20 half-reaction lengths. The temperature and pressure profiles are shown, which permit identification of the gasdynamic evolution and reaction zones separating gases undergoing their induction period from hotter burned gases. Case B of figure 9 corresponds to a single main cellular mode. In the first frame, the triple point is propagating upwards. The bottom part of the leading shock is the Mach shock, while the upper part is the weaker incident shock. Due to the large temperature sensitivity of the reaction rates, the gases shocked by the incident shock remains unreacted and accumulate in a growing tongue shape. As the triple point reflects from the wall in the second frame, a new Mach shock is formed near the top wall and a reflected shock propagates downward. The lower portion of the leading shock is now the decaying incident shock. As the new triple point propagates downward, gas accumulates behind this incident shock as a new layer of unreacted gas. In the fifth frame, the triple point reflects off the bottom wall, and a new Mach shock is formed,

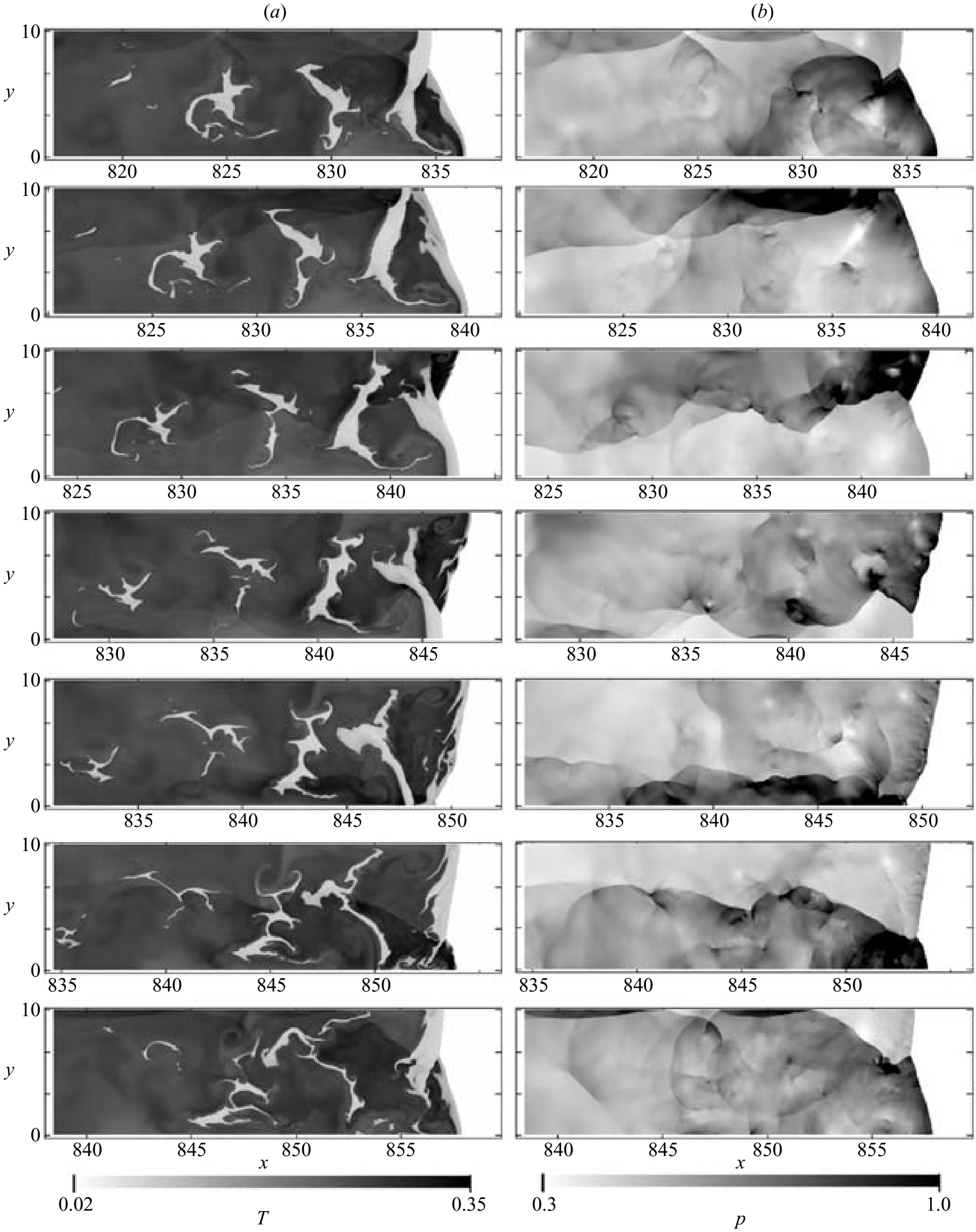

FIGURE 9. Evolution of the temperature (*a*) and pressure (*b*) during one outer cell cycle for $\theta_o = 63.7$ (case B); frames at $t = 701.52$, 705.07, 708.68, 712.17, 715.77, 719.45, 723.21.

which now propagates up. The rapid exothermicity behind the Mach shock and imbalance with the very weak exothermicity behind the incident shock sustains the frontal cellular structure. A sub-structure is also observed superimposed on the main cellular structure, characterized by smaller tongue-shaped structures and triple shock interactions. The origin of this secondary structure was found to correlate mainly with

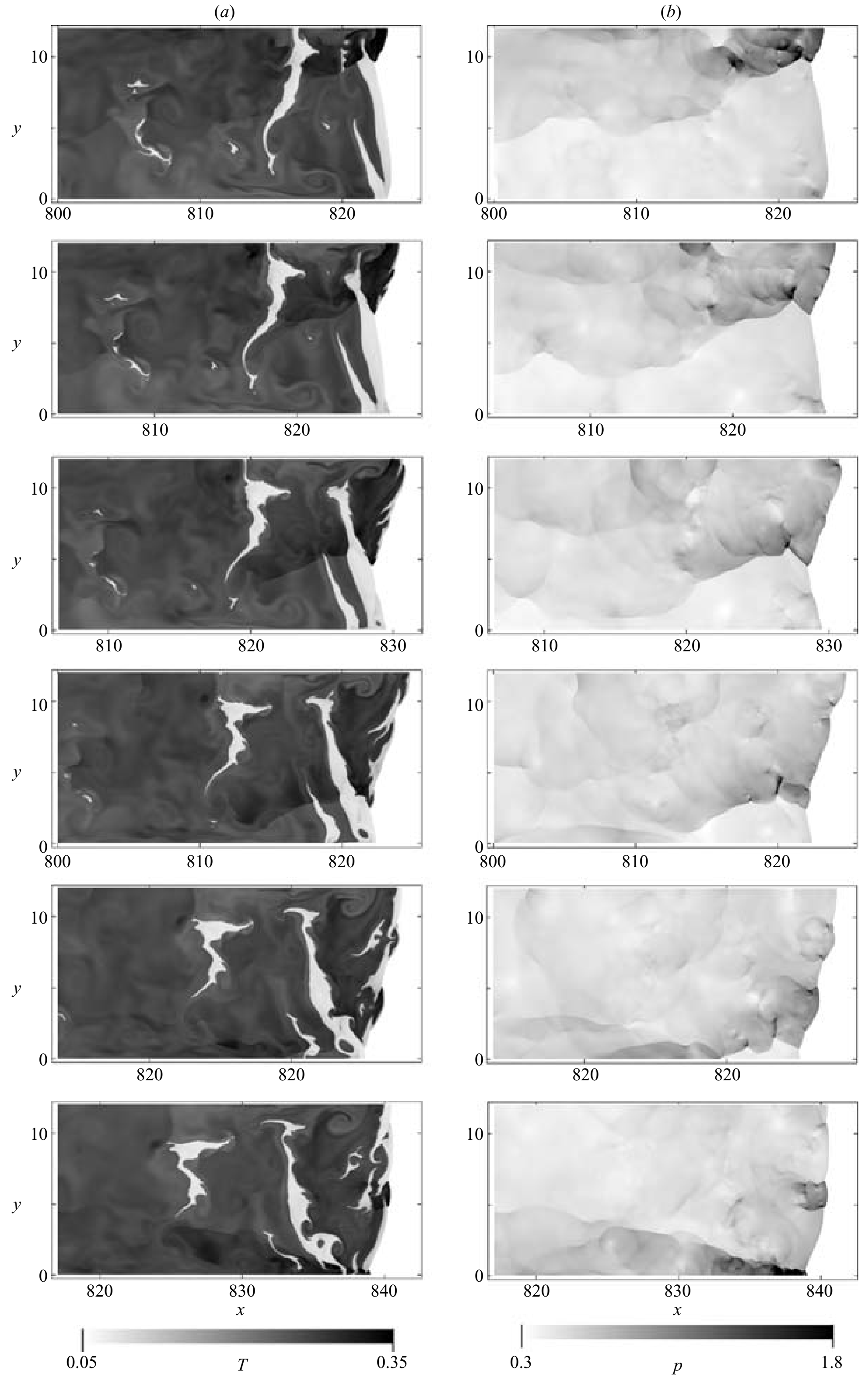

FIGURE 10. Evolution of the temperature (*a*) and pressure (*b*) during one outer cell cycle for $\theta_o = 63.7$ (case A), frames at $t = 690.17$, 693.42, 696.74, 700.26, 703.79, 707.27.

instabilities in the reactive Mach shock at early times, before the decoupling of the reaction zone. Hydrodynamic instabilities also disturb its structure, such as the vortex roll created after the triple-point collision with the wall (or with another triple point).

Globally, since the induction delay of the gas shocked by the incident shock is much longer than the gas shocked by the Mach shock, a layered system is formed behind the detonation front consisting of alternating reacted and unreacted gases, which are convected with the material velocity. These entropy gradients at the boundaries of reacted and unreacted gases maintain the vorticity imparted to them by the cellular frontal structure and deform further through both nonlinear hydrodynamic interactions with transverse pressure waves and through energy addition by reaction. The Kelvin–Helmholtz instability in the shear layers and the Richtmyer–Meshkov instability occurring during the shock refraction at the density interfaces make a reconstruction of the detailed evolution difficult. The resulting randomization of the pressure field is illustrated well in the pressure field evolution, which particularly shows the scattering of the shock system during the interaction with density interfaces at the pocket boundaries. These are very similar to the shock–flame interactions studied extensively by Khokhlov, Oran & Thomas (1999) in the context of deflagration-to-detonation transition studies.

The same physics also operate in the sequence of events illustrated for case A, shown in figure 10, although the details are significantly more complex due to the supplementary active modes in the wider domain. The sequence resembles qualitatively the experimental sequence of figure 7. The temperature and pressure sequence can also be followed on the cellular dynamics of figure 8. In the first frame, the main detonation triple point has just reflected on the top wall, leaving a layer of unreacted gas behind. There is also a weaker mode, which has just reflected on the bottom wall. The first stronger one gives rise to a new unreacted tongue while the triple point propagates downward. Note the instabilities on the shear layer. During this time, the Mach shock structure and reacting gases behind develop their own cellular instabilities, with their own triple-shock interactions, unreacted tongues and unburned pockets of smaller dimension. For example, in the fifth frame, four triple points can be clearly seen on the surface of the main Mach shock. These can also be clearly seen on the cellular record of figure 8.

The weaker mode appearing on the bottom of the first frame is interesting in its own right. Since it is much weaker, its reflection from the bottom wall does not make the leading shock strong enough to radically accelerate the burning rates. Instead, only a small hot spot is created, surrounded by unreacted expanding (and cooling) material. This reacted spot is then convected downstream in the unreacted tongue. Although less frequent, the present calculations also capture pockets of burned gas within pockets of unreacted gas engulfed in reacted gases.

3.4. *The front dynamics*

The pulsations of the front were recorded along the line $y = 0$. From local pressure measurements behind the leading shock the velocity of the wave was deduced via the Rankine–Hugoniot relations. An excerpt of the velocity record is shown in figure 11 for both cases A and B on the interval $700 < x < 1000$. The velocity pulsations can be correlated with the cellular dynamics of the front illustrated in figures 8 to 10 for the flow-field evolution. The sudden increases in detonation velocity or 'spikes' correspond to the triple shock reflections, while the low-velocity excursions correspond to the decoupled stages of the propagation when the incident shock is much weaker than average. The main modes can be correlated with the largest sub-CJ

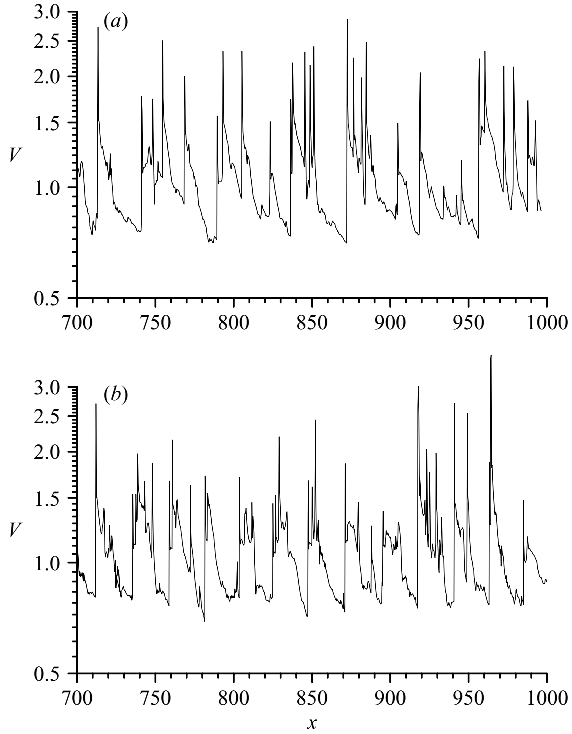

FIGURE 11. Velocity of the leading front recorded along the bottom wall of the computational domain for case A (a) and case B (b).

excursions. Secondary modes can also be observed, corresponding to the secondary cell structure observed on the detonation front, with magnitudes and frequencies of large variability. We have evaluated a power spectrum of the full velocity time series, but were not able to isolate any preferred frequency of oscillation of sub-λ oscillations, although the spectrum is quite noisy due to the small amount of data available. Also noteworthy from the velocity signal is the increased variability in the signal for case A, corresponding to the wider domain. Consistent with the cellular records above, the increased irregularity of the structure leads to a very chaotic signal.

Since the excursions of the leading shock strength from the mean directly affect the local ignition delays, it is worthwhile investigating the probability density function p.d.f. for the leading shock velocity. First, we determined the interval over which the wave is initially overdriven, so that we can choose an interval devoid of this initial transient. Using the time-of-flight data of each minimum in wave velocity, we first determined the time-average velocity of the leading shock for successive outer cell cycles, as shown in figure 12 for case B. After $x \sim 300$, the wave appears to have approached a stationary regime. Figure 13 shows the p.d.f. of lead shock velocity recorded along the bottom wall ($y = 0$) in the interval $300 \leqslant x \leqslant 1000$. It represents the fraction of time the lead shock has the specified value that departs from the ideal detonation velocity of $V = 1$. To obtain the p.d.f., the velocity time series was interpolated at equal time intervals in the stored data. The resulting p.d.f. is found in good agreement between the two runs. The first moment of the distributions, corresponding to the time-average detonation speed, is found to agree with the ideal value within an error of ~1%.

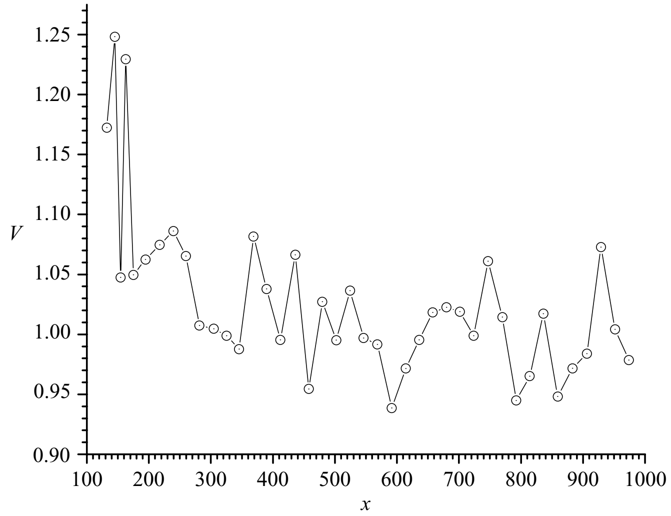

FIGURE 12. Cell-averaged velocity of the leading front recorded along the bottom wall of the computational domain for case B.

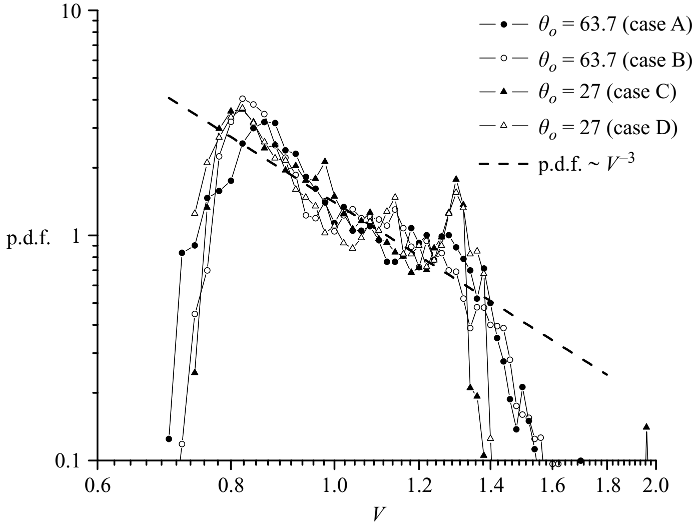

FIGURE 13. Probability density function of the leading shock velocity obtained from the shock velocity time series along the bottom wall for cases A, B, C, and D; broken line shows a power-law dependence with exponent −3. (Cases C and D are described in § 4.)

The shape of the p.d.f. is also interesting. The distribution of shock velocities is highly skewed towards sub-CJ velocities with a minimum of approximately 0.7 of the ideal CJ velocity. The peak of the distribution occurs at approximately $V = 0.8$, consistent with the observations of Austin (2003). This strong skewness can be easily accounted for by the fact that the shock velocity inside the cell always preferentially decays, with very rapid accelerations through triple point interactions. Since the shock spends more time decaying than amplifying, this naturally gives rise to more frequent shock velocities below the average. The overall shape of the p.d.f. can also be inferred by assuming that the local shocks inside the cells decay approximately as cylindrical

Taylor–Sedov blast waves (see, for example, Thomas & Edwards 1983 and references therein) with $V \sim t^{-1/2}$, from which it can be shown that the corresponding p.d.f. of V varies like p.d.f. $(V) \sim V^{-3}$, in good agreement with the data shown in figure 13.

3.5. *The induced exothermicity and local flow-field details*

We further analysed the local flow field in the computations to determine how the leading shock pulsations and the local details of the flow field affect the ignition delays of the processed gas. We have chosen one particular frame and analysed the flow field inside in detail. Figure 14 shows the pressure, density, temperature, reaction progress variable and velocity profiles at one instant in time. This frame is part of the sequence shown in figure 9. The frontal part corresponds to a strong Mach shock at the top portion of the front, while the bottom part is the weaker incident shock. The pressure (figure 14*a*) and velocity profiles (figure 14*e* and *f*) illustrate how the triple-shock structure is maintained, and the direction of the flow behind the transverse shocks and along the shear layer associated with the triple-shock interaction. The density (figure 14*b*) and temperature (figure 14*c*) profiles illustrate the position of the unreacted high-density and cool gases undergoing their chemical ignition process. The distribution of the progress variable α in figure 14*d* also shows that these pockets have a composition very close to unreacted, i.e. $\alpha = 1$. The interested reader can also infer more easily accessible quantitative information from the one-dimensional cuts shown along the lines $x = 840.8$ and $y = 1.5$.

Using the instantaneous field of temperature, the local ignition delay time was estimated by using equation (2.1). The resulting ignition delay field, i.e. the time remaining under steady conditions until the diffusionless explosion time, is shown in figure 15. For reference, the ignition delay behind a shock moving at CJ velocity, in our non-dimensional scales, is

$$t_{e,VN} \cong t_{1/2} = \frac{1}{u_{VN}} = \rho_{VN} = 7.6. \tag{3.15}$$

By inspection of figure 15 and the one-dimensional cuts shown, we see that all the pockets of gas have ignition delays 1 to 2 orders of magnitude longer, and reach values ranging from 100 to 1000, during which the lead front would propagate 100 to 1000 half-reaction lengths. The horizontal cut in figure 15 also shows that the compression by the weak transverse shocks does not shorten the ignition delays of the pockets sufficiently to permit rapid ignition.

The discrepancy between the observed burn out of the pocket on time scales of 20 to 40 and the expected delays based on the diffusionless ignition mechanism is accounted for by the additional diffusion introduced by the numerical scheme, as described above. We investigated its effect on the ‘laminar’ burning rate of the pockets in separate one-dimensional calculations, aimed at determining the burning rate of the pockets from diffusive phenomena inherent in the scheme. The calculation was initialized with a discontinuity in density separating initially reacted and unreacted gases. The initial conditions were chosen as representative of the pocket states (see figure 14), by setting the initial pressure at 0.6 uniformly across the domain and the density to 7.0 and 2.0 in the unreacted and reacted gas respectively. The ensuing numerical flame speed was measured by tracking the location of the flame with respect to the fluid velocity ahead of the flame in the non-reacted material. The calculations were performed for grid resolutions ranging between 32 and 1024 points per half-reaction length. The results are shown in figure 16. For the thermo-chemical parameters used, the flame speed is given approximately by $0.14\Delta x^{0.7}$. The power-law

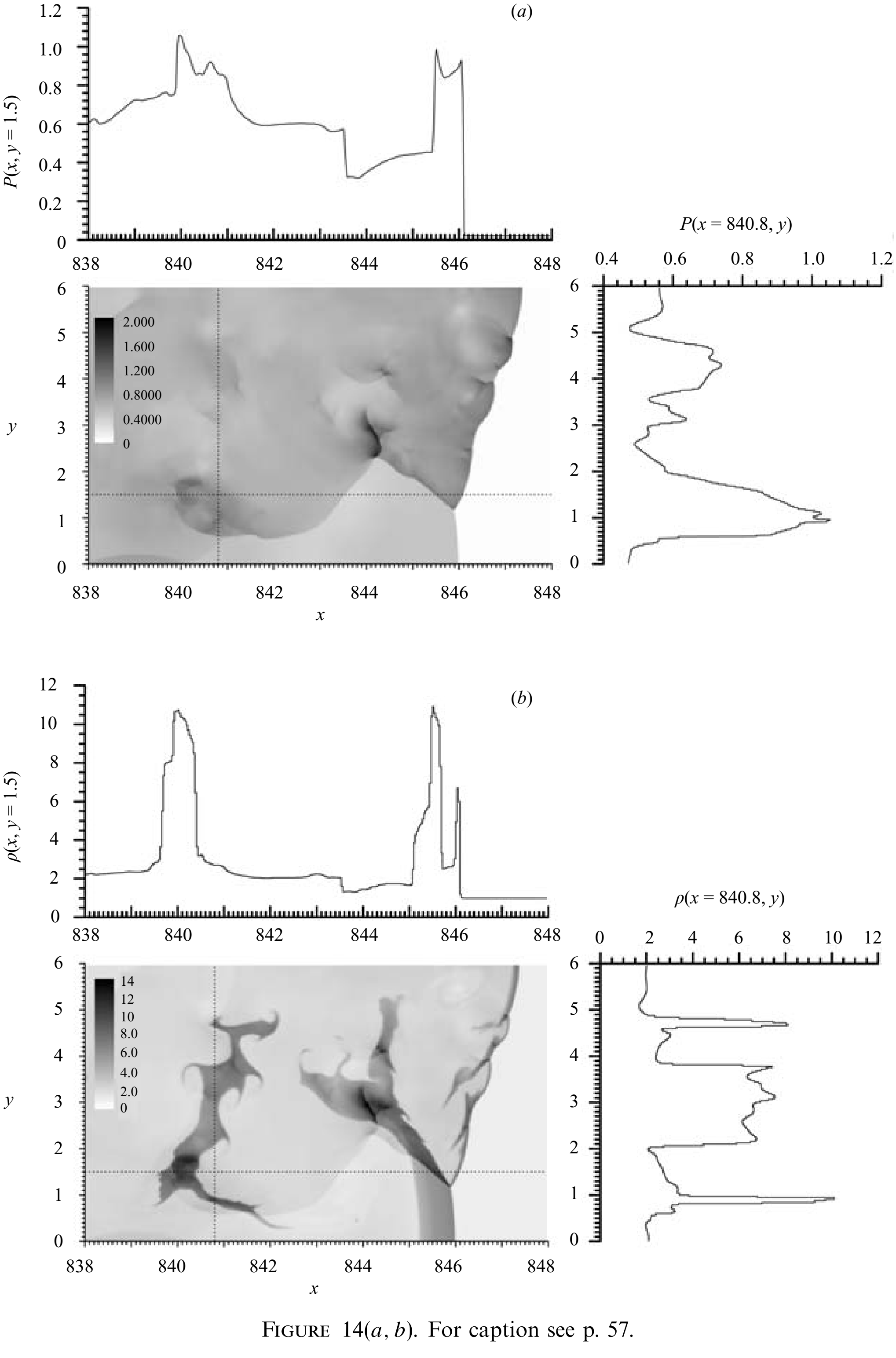

FIGURE 14(a, b). For caption see p. 57.

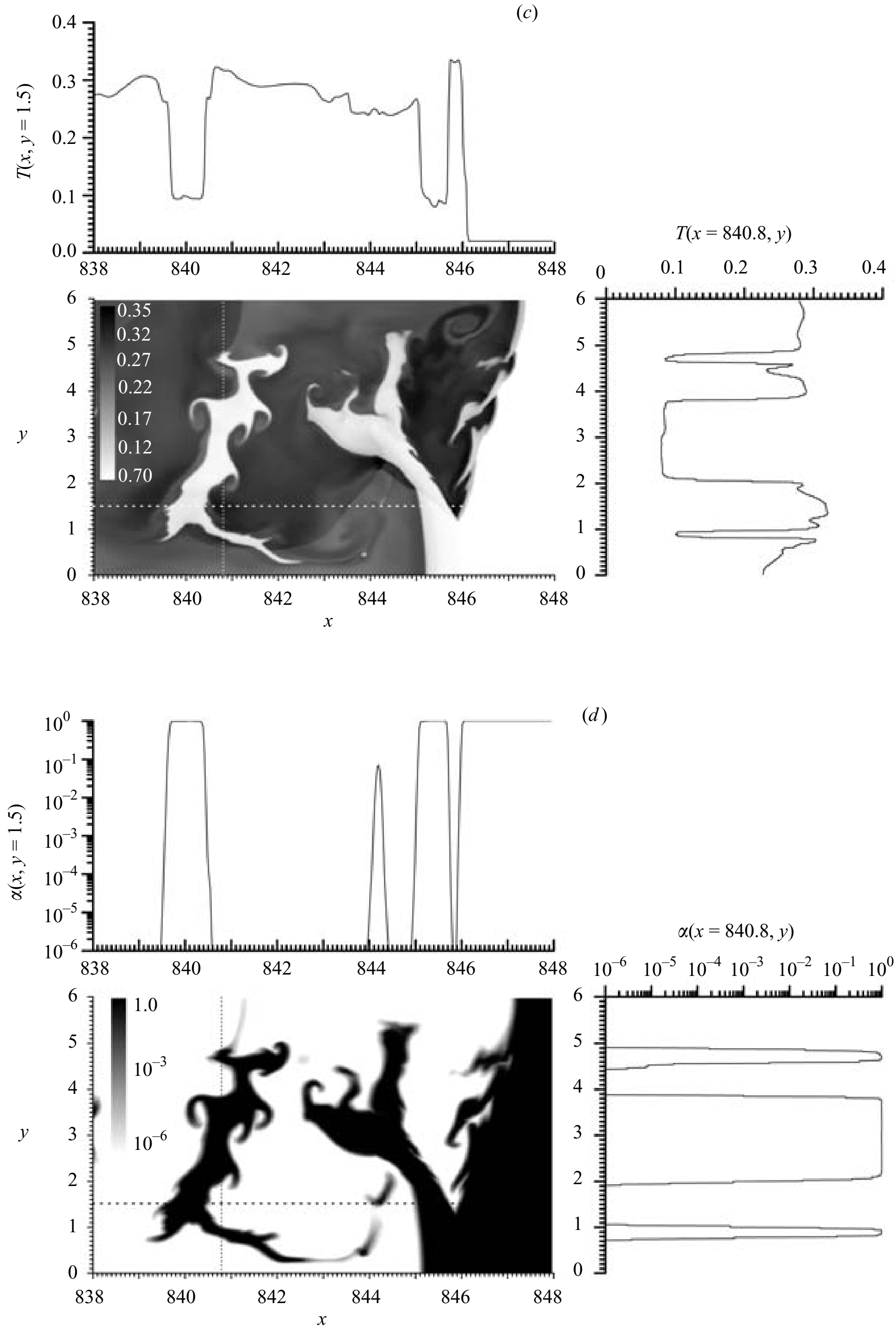

FIGURE 14(c, d). For caption see facing page.

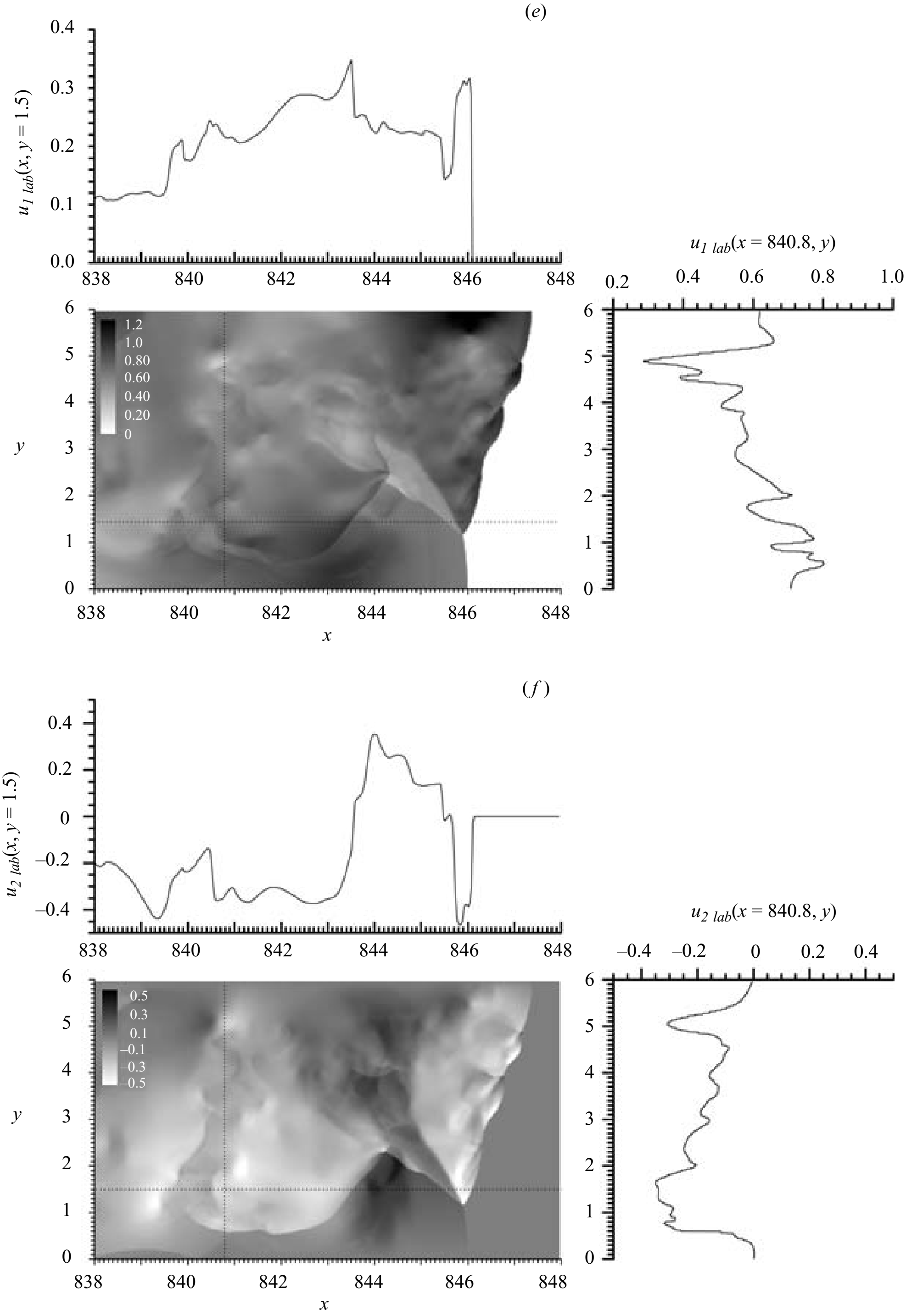

FIGURE 14. Instantaneous pressure (*a*), density (*b*), temperature (*c*), reactant concentration (*d*), longitudinal (*e*) and transversal (*f*) laboratory frame particle velocity for $\theta_o = 63.7$ (case B) at $t = 712.17$; one-dimensional cuts of the flow field illustrate the local details along the lines $x = 840.8$ and $y = 1.5$.

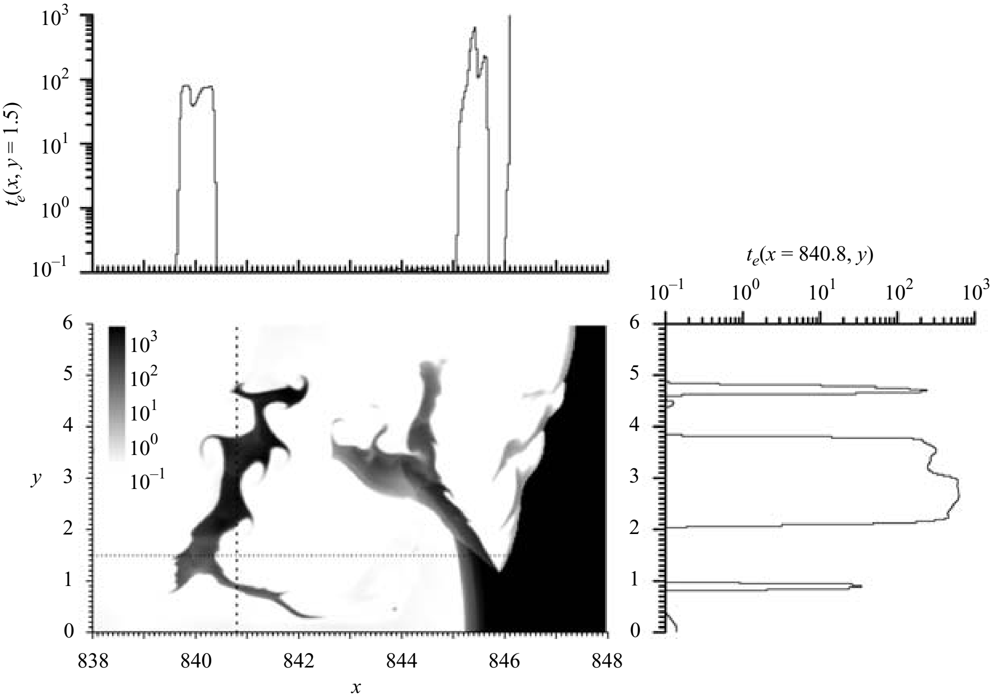

FIGURE 15. Instantaneous ignition delay time of unreacted gas for $\theta_o = 63.7$ (case B) at $t = 712.17$; one-dimensional cuts of the flow field illustrate the local details along the lines $x = 840.8$ and $y = 1.5$; for reference, $t_{e,VN} = 7.6$ in the steady wave

exponent of the dependence on grid resolution is bracketed well by the values deduced from the numerical diffusivity dependence on grid resolution in Falle & Komissarov (1996) (see equation (3.13)). Since the flame speed scales with the square root of diffusivity, a linear dependence of flame speed on grid spacing would correspond to a second-order-accurate solution at the flame discontinuity, while a square root dependence corresponds to a first-order-accurate solution at the discontinuity. The results also demonstrate well how the numerical flame speeds increase with decreasing resolution, which is fully consistent with our resolution studies (see below), which showed a more rapid burnout of the pockets at lower resolutions.

We hence can use the characteristic flame speed computed above to determine how diffusive burning affects the burnout of the pockets on the time scale of their diffusionless ignition in the simulations. For the resolution of 128 points, the numerical flame speed is ~0.004. Assuming a characteristic pocket size of unity, the burnout time of a one-dimensional pocket consumed on both sides by numerical flames at the pocket boundaries separating the burnt from unburnt gas is thus $0.5/0.004 = 125$. This time is comparable with the characteristic ignition delays determined above. Furthermore, shorter ignition times via numerical diffusive mechanisms are expected, since the pocket morphology is multi-dimensional, making our estimate a conservative one. Richtmyer–Meshkov and Kelvin–Helmholtz instabilities further disrupt the pocket morphology and increase their surface area, which leads to a decrease in the burnout time through surface flames, as illustrated above.

It is also useful to compare the results obtained numerically with the experimental flow field. It is found that the pockets in the numerical simulations, although burning

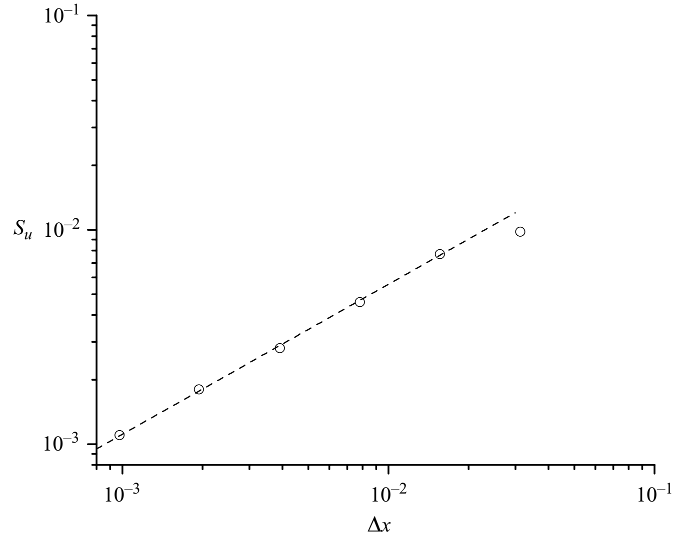

FIGURE 16. Laminar flame speed dependence on grid spacing for $\theta_o = 63.7$; dashed line, power-law fit given by $S_u = 0.14\Delta x^{0.7}$.

faster from surface diffusion, still burn slower than in the experiments by a factor of approximately 5, in spite of the fact that diffusivities in the numerics are larger than the real ones by two orders of magnitude. This may be ascribed to the more important role of turbulent diffusive phenomena in the real experiments, as suggested by the much broader range of scales expected in the experiments than those captured in the numerical simulations.

3.6. *Average structure*

Although the true fine diffusive scales are not attainable in the simulations and a well-characterized turbulent regime is not established owing to large-scale dissipation, we are interested in determining the mean one-dimensional profiles corresponding to such unstable detonations and establishing the role of the fluctuations from the mean large-scale detonation structure. To this effect, the results of the numerical experiments presented above were used to obtain the corresponding one-dimensional time- and space-average representation of the flow field through the detonation wave. We use Favre-averaging, which takes an average weighted by the local density, to account for the changes in density (and momentum and energy density) at different times and positions in space (Favre 1965). Favre-averaging in time and space in the frame of reference of the average detonation motion represents seeking the average properties of many statistically similar Lagrangian fluid elements traversing the detonation wave structure. The mathematical formulation of the Favre-averaging procedure is given in the Appendix.

The spatial and temporal averaging was conducted in the frame of reference moving with the average velocity of the wave. The averaging procedure in the y-direction and in time was performed in the interval $834 < x < 999$, i.e. over 6 cell cycles for both simulations. If x' denotes the coordinate in the frame of reference moving with the average detonation velocity, W is the width of the window for y-averaging and τ is the total time step in averaging, the pressure and density are averaged in the usual way in time and space:

$$\bar{p}(x') = \frac{1}{\tau}\int_{t_o}^{t_o+\tau}\frac{1}{W}\int_0^w p(x', y, t)\,\mathrm{d}y\,\mathrm{d}t, \tag{3.16}$$

$$\bar{\rho}(x') = \frac{1}{\tau}\int_{t_o}^{t_o+\tau}\frac{1}{W}\int_0^w \rho(x', y, t)\,\mathrm{d}y\,\mathrm{d}t. \tag{3.17}$$

The velocity and reaction progress variable α are Favre-averaged by using the result of (3.17):

$$\tilde{u}(x') = \frac{1}{\tau\bar{\rho}(x')}\int_{t_o}^{t_o+\tau}\frac{1}{W}\int_0^w \rho(x', y, t)u(x', y, t)\,\mathrm{d}y\,\mathrm{d}t. \tag{3.18}$$

$$\tilde{\alpha}(x') = \frac{1}{\tau\bar{\rho}(x')}\int_{t_o}^{t_o+\tau}\frac{1}{W}\int_0^w \rho(x', y, t)\alpha(x', y, t)\,\mathrm{d}y\,\mathrm{d}t. \tag{3.19}$$

In the averaging procedure, the time elapsed between successive stored models was applied to weigh each model in the time-average process. We used the entire domain width for y-averaging ($W = 6$ and 12 for cases B and A respectively).

From above, the average detonation velocity was the ideal CJ value estimated with an uncertainty of ∼1%. For this reason, the spatial and temporal averaging was conducted in the reference frame moving with the CJ velocity. The average pressure $\bar{p}$, density $\bar{\rho}$, particle velocity $\tilde{u}$ (in the wave frame), reactant concentration $\tilde{\alpha}$, and flow Mach number are shown in figure 17 for both cases A and B, along with the ideal profiles of the steady ZND structure. First, good agreement is found between cases A and B in terms of the global features, as was also the case for the global flow field obtained above. Close inspection, however, shows subtle differences. The average thermodynamic state in the higher resolution run seems to approach the CJ state at a slower rate. In both cases however, the CJ state is attained at a distance of approximately 40–60, i.e. 50 times longer than in the ideal ZND model. This relaxation to the CJ state was also longer than the burnout time of the pockets, as indicated by the decay of the reactant progress variable α, which occurs on the order of 20 half-reaction lengths.

The flow Mach number in the detonation frame was obtained by assuming that the mean sound speed does not depend on the intensity of fluctuations and is given by

$$\tilde{c}^2 \equiv \gamma\bar{p}/\bar{\rho}. \tag{3.20}$$

In an average sense, it is found that the flow becomes sonic at a distance of approximately 40 to 60. It thus seems that an average sonic surface where $M = 1$ appears at a distance longer than the chemical equilibration, but at a location where the average thermodynamic state of the gas approaches the CJ state.

The Hugoniot diagram representing the mean trajectory in p, $1/\rho$ space is shown in figure 18 for case B. Due to the large fluctuations of the front and the flow within the detonation structure, the state of the particle differs considerably from the ideal Rayleigh line, dictated by one-dimensional conservation of momentum, implying the presence of fluctuations. Nevertheless, as these fluctuations decay, the average path approaches the burned Hugoniot at the ideal CJ point, within the accuracy of our results.

To gain more insight into this relaxation towards equilibrium, which may be responsible for the delayed sonic surface, we monitored the decay of the mechanical and thermal fluctuations from the mean profiles. Following the motion of an

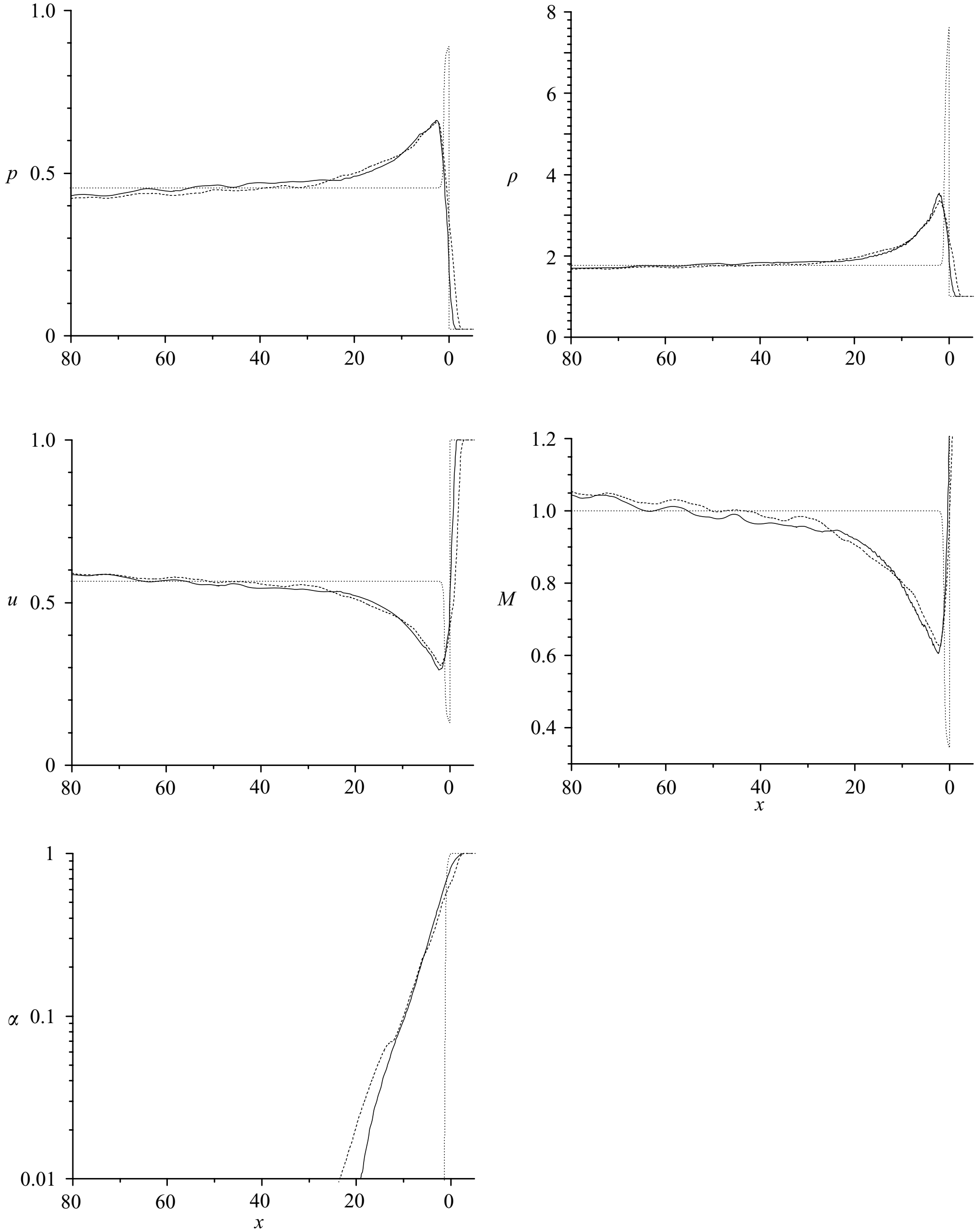

FIGURE 17. Favre-averaged pressure, density, particle velocity, Mach number and reactant concentration profiles for $\theta_o = 63.7$; broken lines, case A; (solid lines), case B; dotted lines, ZND model.

averaged fluid element traversing the detonation wave (see the Appendix), its average momentum and energy are conserved according to

$$\bar{\rho}\tilde{u}^2 + \bar{p} + f = \bar{V}^2 + \frac{1}{\gamma M_{CJ}^2}, \tag{3.21}$$

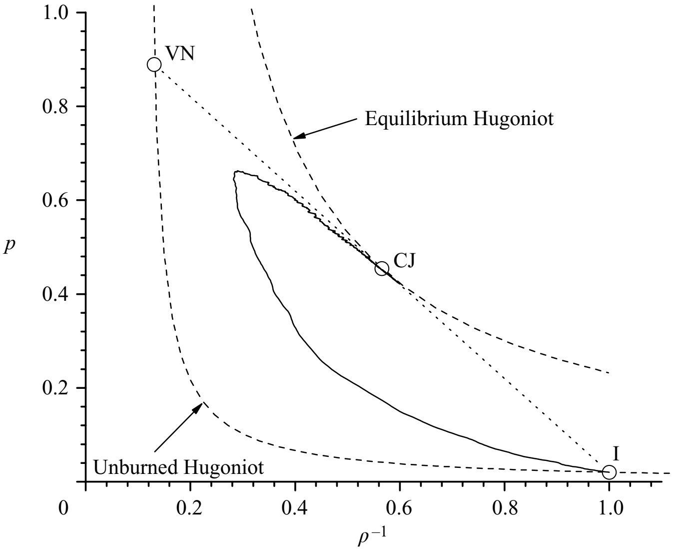

FIGURE 18. The mean path taken by a mean fluid element (solid line) for case B on a P, ρ^{-1} diagram; the dotted line is the ideal Rayleigh line connecting the initial state (I), the shocked von Neumann state (VN) and the Chapman–Jouguet state (CJ).

$$\frac{\gamma}{\gamma-1}\frac{\bar{p}}{\bar{\rho}}+\tilde{\alpha}Q+\frac{1}{2}\tilde{u}^2+\frac{g}{\bar{V}}=\frac{1}{M_{CJ}^2(\gamma-1)}+Q+\frac{1}{2}\bar{V}^2. \tag{3.22}$$

The right-hand sides represent the momentum and energy transported into the detonation structure by the fresh gases, while the left-hand sides represent the instantaneous average values. The explicit dependence of the mechanical fluctuation f and thermal fluctuation $g/\bar{V}$ in terms of fluctuating quantities of pressure, velocity and reaction variable are given in the Appendix (equations (A 31) and (A 32)). Here we are only concerned with the equilibration of the total fluctuations. The terms f and $g/\bar{V}$ represent the residues from the momenta and energies from the mean motion and are explicitly described in the Appendix. They are obtained by evaluating all the terms in (3.21) and (3.22) from the average quantities and subtracting them from the total values on the right-hand-side of (3.21) and (3.22).

The various terms appearing in the conservation of momentum (3.21) and energy (3.22) are shown in figures 19 and 20 for both cases A and B. First, both cases appear to agree well. The momenta partition shows that the mechanical fluctuation f has decayed from approximately 10% close to the front to less than 0.5% of the total at the sonic surface. Likewise, the thermal fluctuations shown in figure 20 also decayed to less than 1% at the sonic surface. Note also that the sonic surface is established after the burnout of the pockets. It thus appears that the location of the sonic surface is best correlated with the decay of fluctuations. Due to limitations in the accuracy of the statistics in the proximity of the sonic surface and to limitations in the physical validity of the grid-dependent fluctuations, we cannot draw more accurate conclusions about the thermodynamic conditions near the sonic surface.

The appearance of the sonic surface after the burnout of the pockets is consistent with the previous experimental findings of Edwards *et al.* (1976), who estimate the location of the sonic surface at several cell sizes λ behind the front. Edwards *et al.* suggest that the dissipation of the energy associated with the transverse wave structure

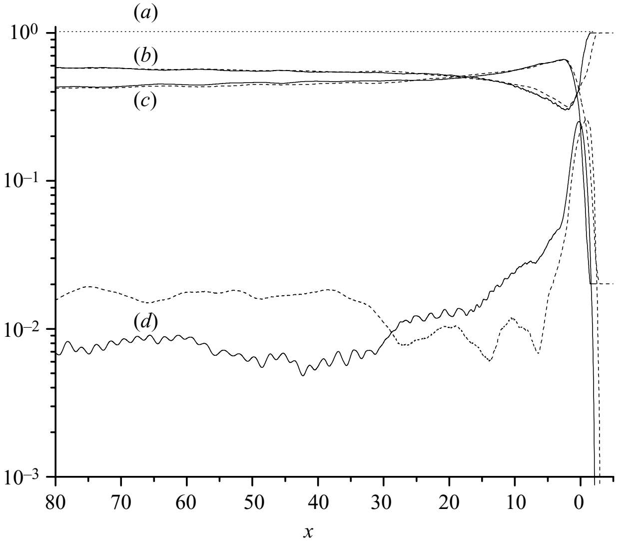

FIGURE 19. Terms in the averaged momentum conservation for case A (broken lines) and case B (solid lines): total momentum $1/\gamma M_{CJ}^2 + \bar{V}^2$(curve *a*), $\bar{\rho}\tilde{u}^2$ (curves *b*), $\bar{p}$ (curves *c*) and f (curves *d*).

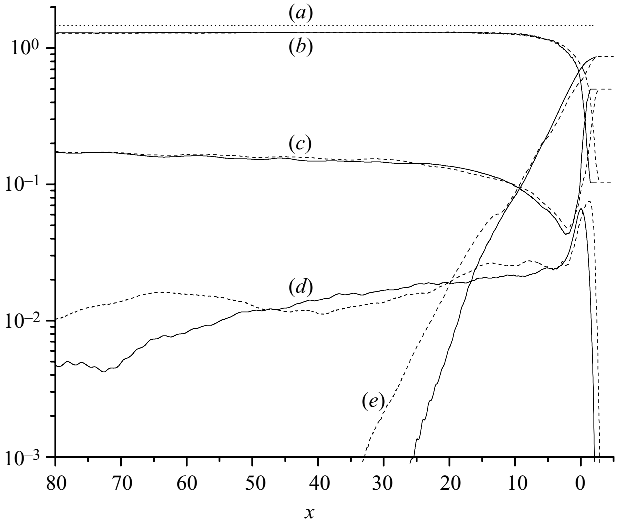

FIGURE 20. Terms in the averaged energy conservation for case A (broken lines) and case B (solid lines): total energy $1/M_{CJ}^2(\gamma - 1) + Q + \bar{V}^2/2$ (curve *a*), enthalpy $\gamma\bar{p}/(\bar{\rho}(\gamma - 1))$ (curves *b*), kinetic energy $\tilde{u}^2/2$ (curves *c*), chemical energy $\tilde{a}Q$ (curves *e*) and turbulent energy $g/\bar{V}$ (curves *d*).

is responsible for this delay in the establishment of a sonic surface, but quote values of turbulent energy much higher than estimated in the present study from the numerical simulations. Qualitatively, the results of the present study support their hypothesis for the delayed sonic surface. A quantitative comparison between experiment and simulations is not possible at present due to the limitations in capturing correctly the turbulent energy amplitude and its dissipation. Such a comparison would require the proper calculation of the turbulent dissipation behind the detonation wave, to be performed in three dimensions, such that the Kolmogorov cascade and the correct small-scale dissipative processes, apart from imbedded shocks, are properly addressed. However, this would represent a formidable computational challenge.

4. The structure of weakly unstable detonations

The second series of computations focused on detonations for which the chemical reaction rate is much less sensitive to temperature fluctuations. For such detonations, the detonation cellular dynamics are more regular. These have been extensively studied in the past in numerical simulations (e.g. Sharpe 2001; Deiterding 2003; Hu *et al.* 2005) and experiments (Edwards *et al.* 1970; Pintgen *et al.* 2003). We wish however to determine their average detonation structure in the same framework as above. This can help us draw conclusions by comparison with the results obtained above. The activation energy was reduced by approximately a factor of 2 to a value of $\theta_{VN} = 5.6$ (corresponding to $\theta_o = 27$). The heat release and isentropic exponent were set to $\beta_{VN} = 10.4$ (or $\beta_o = 50$) and $\gamma = 1.2$. These parameters correspond to one-dimensional detonations characterized by a single unstable nonlinear mode of pulsation, for which the activation energy is lower than the critical value giving rise to chaotic dynamics (Ng *et al.* 2005*a*). This range of activation energies is characteristic of mixtures such as hydrogen, acetylene and carbon-monoxide at low pressures (Radulescu 2003; Austin *et al.* 2005; Ng *et al.* 2005*b*), which are characterized by regular cellular structures. For these mixtures, the experimental results indicate that turbulent diffusive burning is not expected to play a major role (Radulescu & Lee 2002; Pintgen *et al.* 2003), unlike the highly unstable cases, and hence we have a better chance of capturing the main features of this regular cellular structure in the numerical simulations.

The width of the computational domain was set to a value of 10, to isolate a single-mode detonation. The length of the domain was set greater than 1000. Due to the smaller sensitivity of the reaction rates, it was found that the detonation can be initiated much more easily. A high-pressure region of width 2, pressure 5 and density 1 was used to directly initiate the detonation via a strong reacting blast wave. The strength of the ‘igniter’ was chosen to ensure the most direct transition to a self-supported detonation; a larger amount of energy would overdrive the wave over longer distances, while a weaker source would either prevent initiation or give rise to long initiation transients. Resolution levels of 32 and 64 points per half-reaction length were used, henceforth denoted as cases C and D. The numerical technique was the same as described above.

Figure 21 shows the cellular structure obtained by the time-integrated exothermicity for the two cases C and D. This illustrates the very similar dynamical behaviour obtained in both cases, with the detonation front having a very regular quasi-periodic cellular structure. Note that apart from a different initiation transient, which is affected by resolution, both resolution levels provided the same wave dynamics. Figure 22 shows the detonation velocity profile recorded on the bottom wall of the domain. Likewise, a very regular pulsating profile is obtained, which appears to be stabilized to a limit-cycle behaviour at distances greater than approximately 400. A low-frequency modulation is still observed with wavelength equal to approximately 10 cell cycles, which may be due to the initiation transient. Note also that the results of both resolutions appear to have converged to the correct period and amplitude, although the growth rate of the instability during the initiation transient differs, and creates a lag in the pulsations. Also shown in figure 22 are the cell-averaged velocities

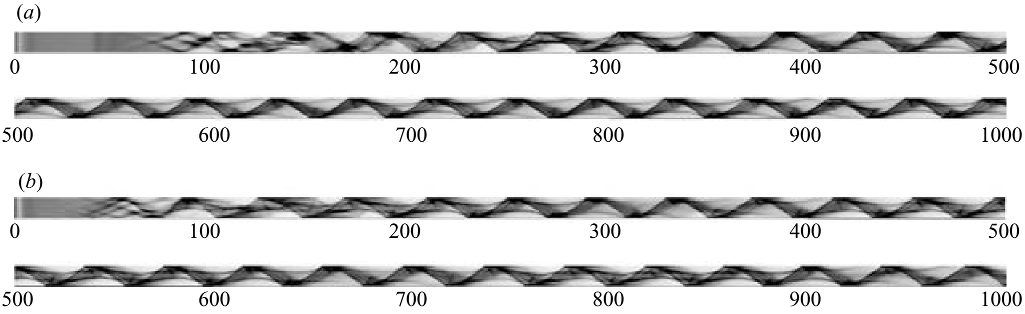

FIGURE 21. Time-integrated exothermicity illustrating the cellular structure for the $\theta_o = 27$ detonation for cases C (*a*) and D (*b*).

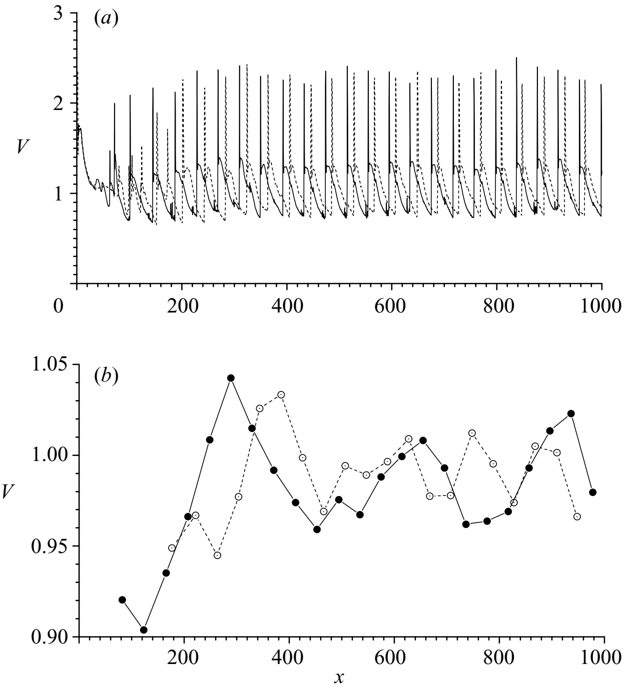

FIGURE 22. Velocity of the leading front recorded along the bottom wall of the computational domain (*a*) and (*b*), cell-averaged velocity for cases C (broken line) and case D (solid line).

obtained from the time-of-flight data at each cell apex. We chose the last 10 cell cycles to compute the time-averaged detonation velocity by simply taking the ratio of the distance travelled over the time required to travel that distance. The average detonation velocity was found to be 1% and 0.8% below CJ for respectively the 64-point and 32-point resolution cases, estimated with a standard deviation of 1.6% from the individual cell time-averaged values.

The p.d.f.s of the velocity signals for both cases C and D are shown in figure 13. They seem to agree very well with the p.d.f.s of the highly unstable detonation, with most probable shock velocity of $V^* = 0.8$ and minimum of 0.7. Some of the high-velocity excursions observed for the unstable detonations are not reproduced however.

4.1. *The flow field*

Figure 23 shows four frames in the evolution of the temperature and pressure profile during a time interval of approximately 20, corresponding to half a cellular cycle. It is also interesting to follow the same evolution on the cellular record of figure 21 and the velocity of the leading shock measured on the bottom wall shown in figure 22. In the first frame, the triple point is approximately in the centre of the channel and is propagating up. In the last frame, the triple point is propagating down. At this point, the flow field is almost identical to the first frame, but reversed horizontally, and marks the end of half of a cell cycle.

The temperature field shows the formation of unreacted pockets, which form by the same mechanism as considered above. The pressure field illustrates the shock structure. The global details of the flow field computed are found in good agreement with experimental results of Edwards *et al.* (1970) of mode 1 detonations in carbon-monoxide with oxygen, which showed with unprecedented clarity for the first time the unburned layers of gas cut off from the main front following the triple shock collision with a wall, although these were misinterpreted at that time.

In the first frame, a growing tongue of gas extends downward, corresponding to gas shocked by the incident and reflected shock at an earlier time. This layer extends as a counterclockwise vortex at the bottom with alternating layers of gas shocked by the Mach stem and gas shocked by the incident shock, which is reacting much slower. This gives rise to a roll-up structure. In the second frame, the triple point has reached the top wall and the rollup structure has grown, as more gas reacted and gave rise to volumetric expansions. Between the second and third frame, the triple point reflected from the top wall, resulting in two forward and backward jets of material. In the forward motion, a new Mach stem is formed, along with the vortex described above. In the backward direction, the previous tongue is separated from the front as an unreacted pocket, which is deformed by the jetting action and the passage of the reflected shock. As the flow field evolves, the unreacted pocket falls further behind the main front, convected at the local fluid velocity. It is consumed at a distance of approximately 15 and after a time of approximately 30 after first being shocked by the incident shock of the front. Its evolution can be traced by taking advantage of the quasi-periodicity of the flow without too much difficulty. Figure 23 also shows the evolution of the simultaneous pressure field, illustrating the transverse pressure waves equilibrating downstream, the details of the shock refraction process at the pocket boundaries, the reflected pressure waves at the tongue interfaces and the triple point reflection process at the wall. Even in this regular-structure detonation wave, the details of the interactions are very complex.

One interesting feature observed in the simulations, but not in the experiments of Edwards *et al.* (1970) on the detonation structure, is the result of the interaction of the vortex rings created by transverse wave collision with the gases behind the Mach stem and the resulting formation of a ‘jelly-roll’-like structure of unreacted gases wrapped by hot reacted and reacting gases. The origin of this discrepancy is not clear at present, although it may be a signature of the important role of diffusive processes in the fine-scale alternating layers of material driven by triple shock collisions.

In these simulations, although small-scale dissipation is still active, most of the gas reacts after its diffusionless ignition delay. The spatial distribution of the instantaneous ignition delay is shown in figure 24, obtained from the temperature field of the first frame of figure 23 via equation (2.1). The longest ignition delay corresponds to the gas shocked by the incident shock, with values $\sim$30. The gas in the unreacted tongue and

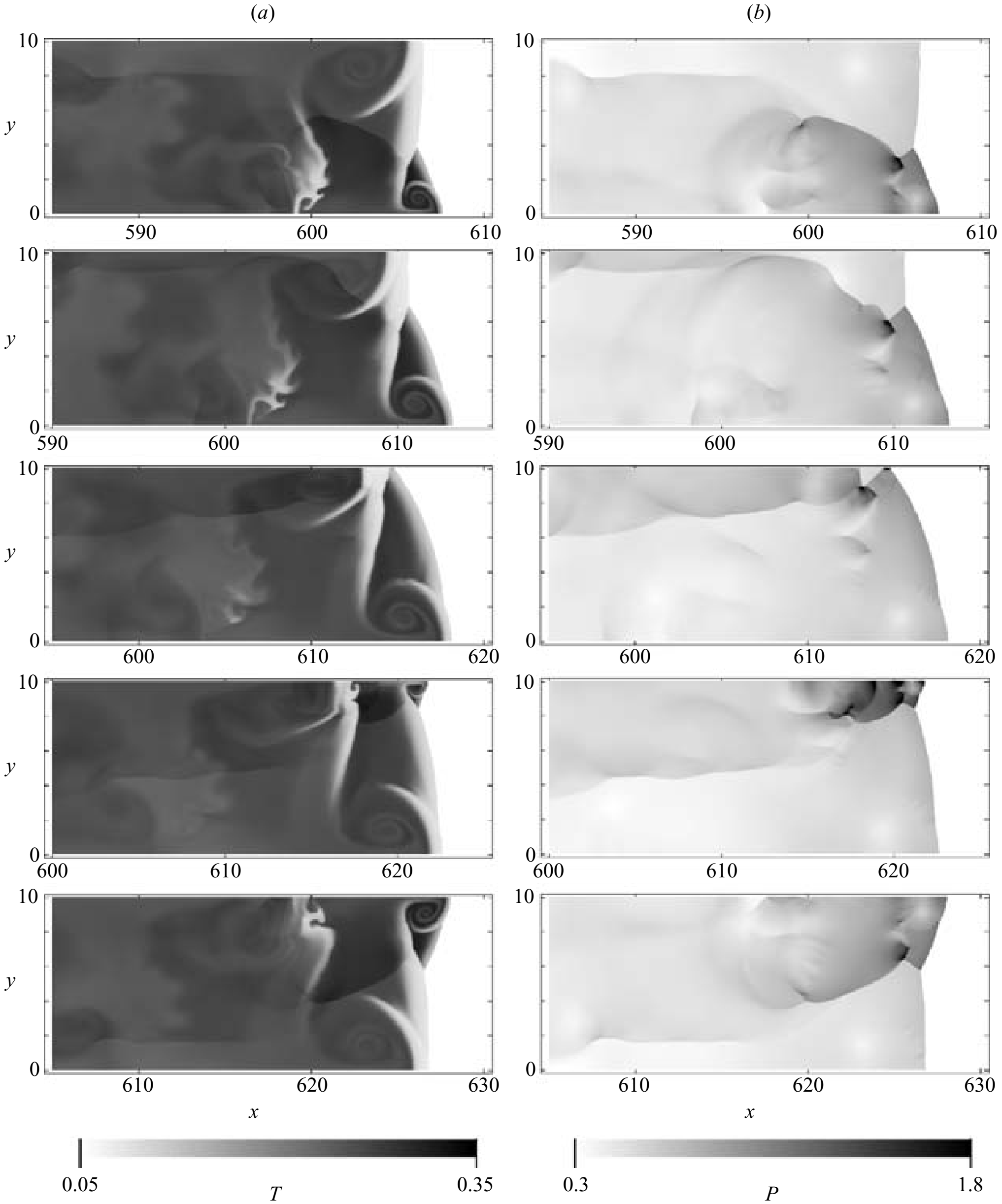

FIGURE 23. Evolution of the temperature (a) and pressure (b) during half a cell cycle for $\theta_o = 27$ (case D); frames at t = 610.03, 615.14, 620.21, 625.29, 630.45.

in the separated pocket has ignition delays of less than 10. For reference, the ignition delay in the steady wave is $t_{e,VN} = u_{VN}^{-1} = \rho_{VN} = 8.7$. Considering the temporal evolution of the flow field illustrated in figure 23, we see that all the unburned gas ignites with the appropriate diffusionless times, as expected. These considerations indicate that diffusion effects play a minimal role in such weakly state- sensitive detonations. In contrast with the simulations above for the highly unstable detonations, this is due to the fact that in spite of the fluctuations, the characteristic ignition delays

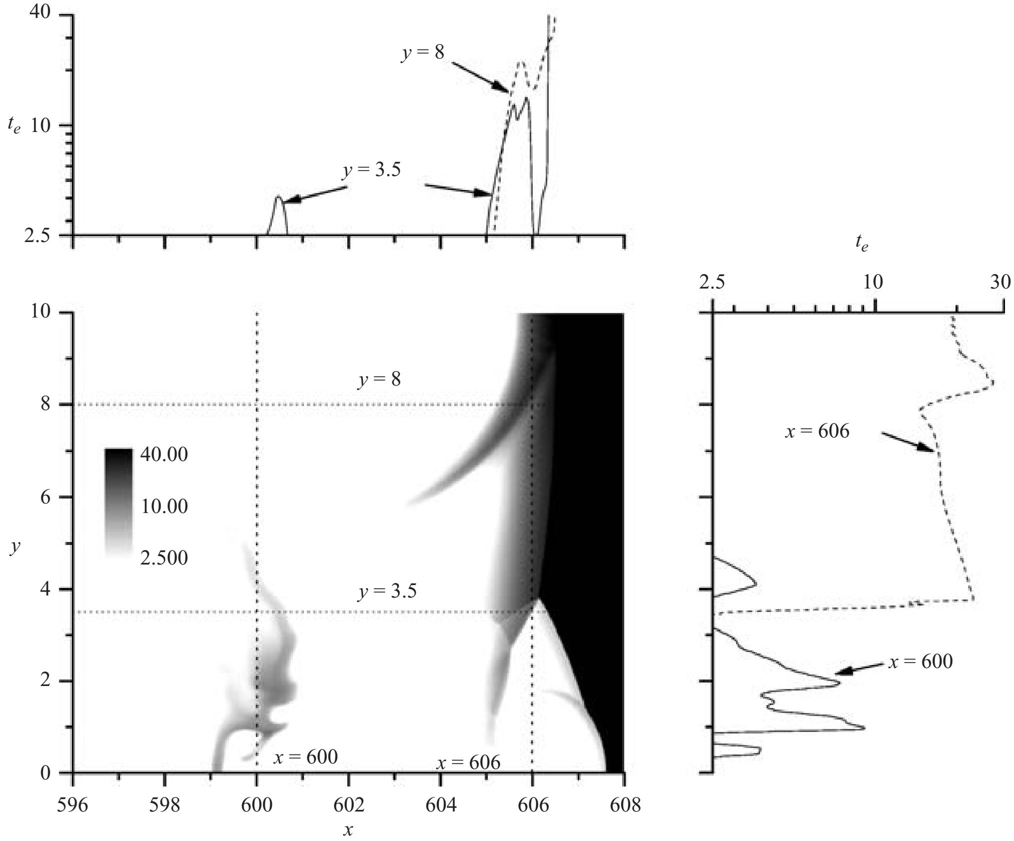

FIGURE 24. Instantaneous ignition delay time corresponding to the first frame of figure 22 ($t = 610.03$) and two-dimensional cuts along ($x = 600$, 606 and $y = 3.5$, 8); for reference, the ignition delay in the steady wave is $t_{e,VN} = 8.7$.

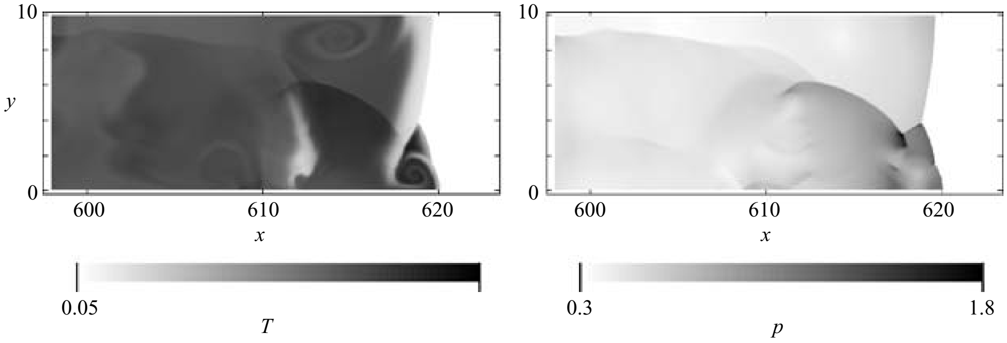

FIGURE 25. Temperature and pressure profiles for $\theta_o = 27$ (case C) at $t = 618.49$.

are still much shorter than those over which the prescribed (numerical) diffusion operates.

We also verified the convergence of our results. Figure 25 shows the temperature and pressure evolution obtained at a lower resolution (case C), at a time corresponding to approximately the same stage in its evolution as the first frame of figure 23. In spite of the global retardation of the entire cellular cycle (originating from the initiation transient), we see that most features agree between the two sets of simulations, with a slightly higher rate of reaction in the lower-resolution run, consistent with the effect of dissipation on the burning rates. A more quantitative analysis is performed below when comparing the average reaction rates.

4.2. *Average profiles*

The average reaction zone structure for both the 32-point and 64-point resolution runs was determined in the last 10 cell cycles. At each successive time step, the y-averaged solution was obtained. The time-average solution was then continuously updated at each successive time step. The average wave velocity used was 0.99 and 0.992 for the 64- and 32-point resolution levels respectively, as determined above. The Favre-averaged reaction zone profiles for pressure, density, velocity (in the coordinate system moving with the average speed of the detonation), reaction progress variable and flow Mach number are shown in figure 26 along with the ideal ZND solution.

Close inspection of the average reactant concentration profiles for the different resolutions shows that the reactant is consumed somewhat slower in the higher-resolution run. This is consistent with the effect of numerical dissipation controlling the burnout rate of the pockets from the edges at lower resolutions. The slower burnout rate in the higher-resolution run, which approaches the true diffusionless burnout rate, is responsible for the lower equilibration rates of the various profiles towards the CJ values. For the 64-point resolution simulation, an average sonic surface is developed at a distance of approximately 21, while at the lower resolution, the sonic surface appears at a distance of $\sim$10. In both cases however, the average pressure, density and velocity approach the ideal CJ state at the sonic plane.

A second feature characteristic of the average profiles is the compression wave travelling behind the sonic surface. Over the interval used for the averaging, we find that the position of this average compression wave is stationary, hence propagating at a velocity comparable with the average detonation in the absolute frame. Its position is also found to be quite different in the two resolution simulations. The origin of this compression wave may be due to a number of reasons, possibly a consequence of the initiation transient, which is different in the two simulations owing to the growth rate of the cellular instability. Nevertheless, by virtue of the sonic surface, it is outside the average domain of influence of the leading front, and does not influence the detonation propagation.

The average path taken by a fluid element traversing the detonation structure in the (p, ρ^{-1})-plane from the initial state to the sonic surface is shown in figure 27 for the higher-resolution simulation. In spite of the weaker instability, the structure still departs significantly from the ideal structure. This may be due to the fact that the shock pulsations do not differ considerably, as indicated by the p.d.f.s of the lead fronts. However, the rate of equilibration is significantly different, as indicated above. From the inset of figure 27, one can see that the gas state at the sonic surface lies somewhat below the ideal CJ state, suggesting that perhaps the detonation is of the eigenvalue type (Fickett & Davis 1979), corresponding to non-equilibrium at the sonic plane. To verify whether this is the case, the decay of mechanical and thermal fluctuations in the Favre-averaged conservation equations for momentum (3.20) and energy (3.21) were estimated in the same manner as for the highly unstable detonations. The various terms in the averaged one-dimensional momentum equation are shown in figure 28 for two different resolutions. The terms appearing in the energy equation are shown in figure 29. The magnitude of the various terms is comparable

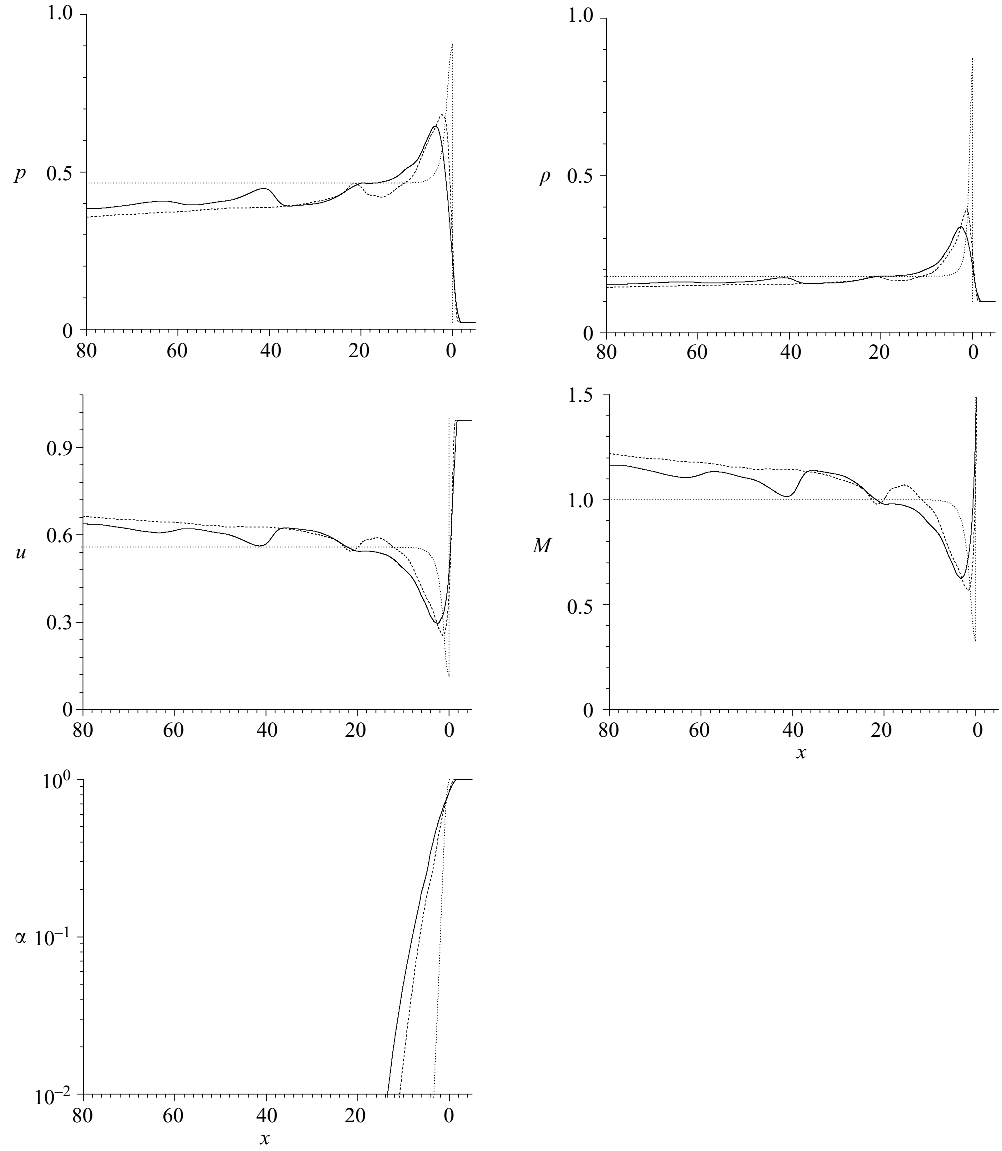

FIGURE 26. Favre-averaged pressure, density, particle velocity, Mach number and reactant concentration profiles for $\theta_o = 27$; broken line, case A; solid lines, case B; dotted line, ZND model.

with those of the highly unstable detonation of figures 19 and 20. It is found that the magnitude of the mechanical fluctuation f has a maximum of 30% at the front and decays to approximately 1% at the sonic plane. The magnitude of the turbulent energy $g/\bar{V}$ estimated from the difference of the total energy available and the mean enthalpy, kinetic and chemical energies peaks at approximately 5% of the total energy and slowly decays to approximately 0.5% at the sonic plane. A negligible fraction of chemical energy is observed at the sonic plane. The same levels in the fluctuating terms are also observed for the lower-resolution case, although the relaxation rates are more rapid, consistent with the increase dissipation at lower resolutions.

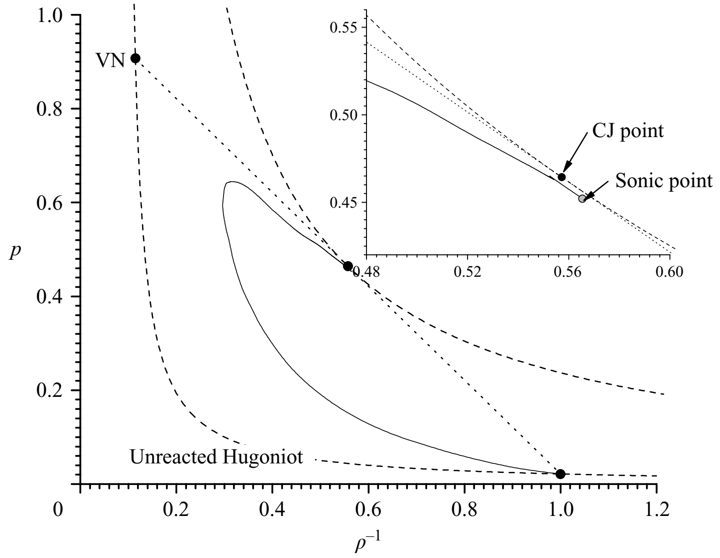

FIGURE 27. The integral curve of a mean Lagrangian particle traversing the detonation wave structure on a p, ρ^{-1} diagram for $\theta_0 = 27$ (solid line), unreacted and equilibrium Hugoniot (dashed line), and the ideal Rayleigh line (dotted line); inset shows a magnified view in the vicinity of the average sonic plane.

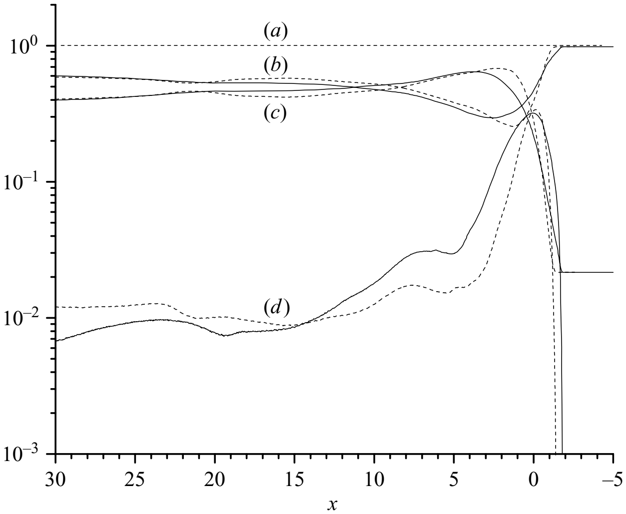

FIGURE 28. Terms in the averaged momentum conservation for case C (broken lines) and case D (solid lines): total momentum $1/\gamma M_{CJ}^2 + \bar{V}^2$(curve *a*), $\bar{\rho}\tilde{u}^2$ (curves *b*), $\bar{p}$(curves *c*) and f (curves *d*).

At the higher resolution, the results also illustrate that the sonic plane is established at a somewhat greater distance than where the chemical energy release ends. However, the difference is not as large as for the high-activation-energy detonations treated above. This may be due to differences in the form of exothermicity profiles in the two cases. At high activation energy, the one-step Arrhenius reaction is characterized by an exothermic period of much shorter duration than for the lower activation energy,

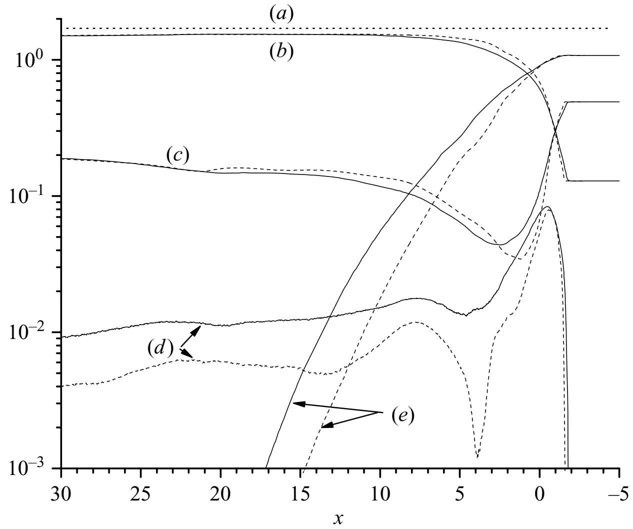

FIGURE 29. Terms in the averaged energy conservation for cases C (broken lines) and D (solid lines): total energy $1/M_{CJ}^2(\gamma-1)+Q+\bar{V}^2/2$ (curve *a*), enthalpy $\gamma\bar{p}/(\bar{\rho}(\gamma-1))$ (curves *b*), kinetic energy $\tilde{u}^2/2$ (curves *c*), chemical energy $\tilde{\alpha}Q$ (curves *e*) and turbulent energy $g/\bar{V}$(curves *d*).

keeping other scales constant. In this sense, the dissipation of fluctuations in the present low-activation-energy simulations may be masked by the slow exothermicity of the chemical process.

Since the detonations considered here were much more regular, permitting much more resolved statistics for each resolution, we also verified if the detonations obtained are compatible with the generalized CJ condition in the presence of source terms due to generation and dissipation of fluctuations (Nikolaev & Zak 1989), in direct analogy with the work performed on eigenvalue detonations in the presence of other source terms (see Fickett & Davis 1979 for details). Differentiating the conserved mass, momentum and energy conservation equations following an averaged fluid particle (equations (A 31) and (A 32) in the Appendix) with respect to time, upon re-arrangement, one obtains the so-called *Master* equation for the fluid element acceleration:

$$\bar{\rho}\frac{\mathrm{d}\tilde{u}}{\mathrm{d}t}=\frac{\gamma\tilde{u}(\mathrm{d}f/\mathrm{d}t)-(\gamma-1)(\mathrm{d}g/\mathrm{d}t)-(\gamma-1)\bar{V}Q(\mathrm{d}\tilde{\alpha}/\mathrm{d}t)}{\bar{c}^2-\tilde{u}^2}\equiv\frac{\Phi}{\eta}, \qquad (4.1)$$

where the time t is taken as independent variable instead of the spatial location of a fluid element x. This equation represents the effect of the relaxation of mechanical fluctuations, thermal fluctuations and chemical fluctuations which act to accelerate or decelerate the averaged low in the reaction zone, and hence compete in the attainment of the sonic condition. By inspection, the solution is singular at the sonic surface, where $\eta=0$. The unique solution for the reaction zone structure is obtained by requiring that simultaneously $\Phi=0$, constituting the *generalized CJ criterion*. The generalized CJ criterion is satisfied for only a specific detonation wave velocity, which is the 'eigenvalue' that will permit a singularity-free structure.

Figure 30 shows the thermicity Φ and the three terms of equation (4.1) for both the 32-point per half-reaction length and 64-point per half-reaction length simulations. It is found that the chemical and thermal relaxation effects compete with the mechanical

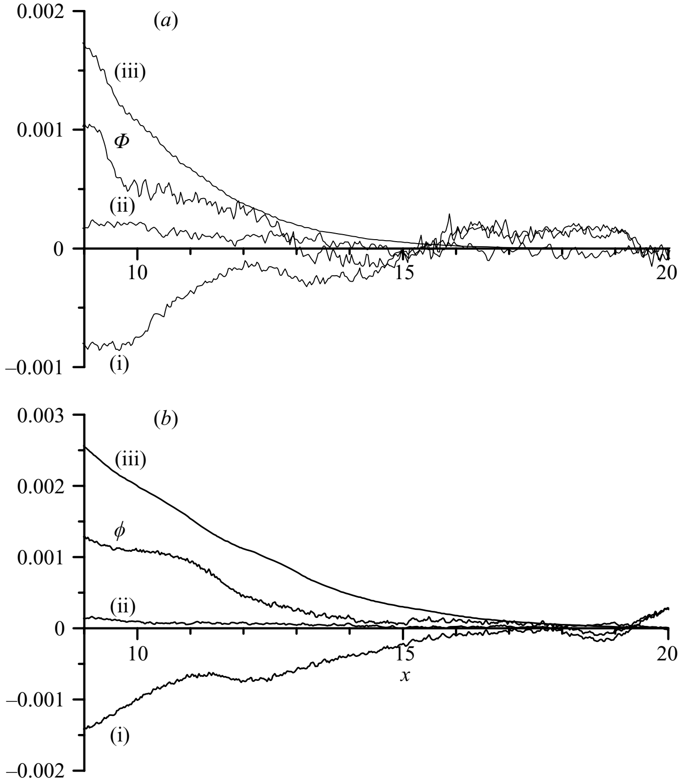

FIGURE 30. The terms in the total thermicity (Φ) equation for cases C (*a*) and D (*b*): [$\gamma\tilde{u}(\mathrm{d}f/\mathrm{d}t)$] (lines i), [$-(\gamma-1)(\mathrm{d}g/\mathrm{d}t)$] (lines ii), and [$-(\gamma-1)\bar{V}Q(\mathrm{d}\tilde{\alpha}/\mathrm{d}t)$] (lines iii).

fluctuation decay, consistent with the sign of the terms in equation (4.1) (see also the Appendix). The terms balance out at approximately $x \approx 20$ and 13 for the 64- and 32-point simulation respectively, in good agreement with the position of the sonic surface established at $x \approx 21$ and 12 respectively. Thus, the generalized CJ criterion appears to be verified for these weakly unstable detonations. Whether the rear of all cellular detonations is always dictated by an eigenvalue structure is not clear at present and clearly much more-resolved detonations would be required, with the physical turbulent transport replacing the artificially high diffusivities used in the present simulations.

5. Further discussion

The detailed comparison of real and numerical simulations of highly unsteady detonations have revealed that the average chemical thickness observed in the experiments cannot be rationalized based on diffusionless ignition alone. Even when supplementary diffusive fluxes were introduced in the numerical code, to provide the burning mechanism for the unreacted pockets, the global computed reaction time was still much longer than in the experiments. Our experimental evidence and results of the computations clearly show the potential role played by Kelvin–Helmholtz and Richtmyer–Meshkov instability in enhancing the mixing and burning rates. Furthermore, considering the recent results of the simulations of Arienti & Shepherd (2005) of ignition along an unsteady diffusion layer characteristic of detonation triple points, it appears that even modest increases in scalar dissipation rates can account for the promoting effect of diffusive phenomena in detonations.

However, in spite of these results highlighting the necessity of ever-increasing computational resources to accurately compute unstable detonation waves, the present study also demonstrated quite conclusively that an average detonation structure is a meaningful concept that allows rationalization of the detonation wave velocity, the global rate of energy release inside the structure and the location of the sonic surface. The results of the present study also illustrate the important role of fluctuations. The partition of the available momentum and energy into fluctuating components and the further dissipation of this energy verified previous experimental findings of Edwards *et al.* (1963, 1976) on delayed sonic surfaces with respect to the surface where the chemical reaction was deposited in the flow. However, the amount of energy contained in these fluctuations was found to be of the order of 1% by the time all the chemical energy was deposited in the flow. As this represents quite a small fraction of the available energy, the dissipation process following the chemical energy release seems of less importance to the dynamic properties of the detonation waves, such as initiation requirements and failure limits (Lee 1984). For these phenomena, a much more important rate process is the rate at which energy is being deposited to the flow. It thus follows that a simplified detonation model should capture the correct energy addition rate.

The results obtained in the present study suggest that the average structure of detonations is well-approximated by a one-dimensional description, provided the generation and decay rates of the fluctuations are explicitly formulated in order to satisfactorily account for the reaction zone structure and location of the sonic surface. The competition between these relaxation rates determines the location of the sonic surface. It thus follows that a purely empirical framework involving a relaxation formalism can be sought to characterize the cellular structure of detonations by simply specifying empirical relaxation rate laws for the chemical, mechanical and energetic relaxation processes towards equilibrium. The various (postulated) relaxation rate terms in the assumed equations can be calibrated against real or numerical experiments for the structure. When properly calibrated, this can give the desired predictive model for the detonation structure and dynamic parameters.

For the weakly unstable detonations, closure also appears possible without invoking small-scale turbulent effects. For this type of mixture, our results indicate that only the large-scale fluctuations from the average profiles associated with the large-scale cellular dynamics are important. Cellular gasdynamic models could be constructed based on the flow field inside the cells. However, the modelling of the highly unstable detonations presents significant difficulties, since turbulence at fine scales is likely to play a crucial role in the gas ignition mechanism. At present, such closure models are unavailable. Large-eddy-simulation models of highly compressible reacting turbulence are unavailable. Current turbulence models for deflagrations (e.g. see Peters 2000), which are based on the low-Mach-number approximation, are inadequate due to their failure to address the compressibility effects important in the reaction zone of cellular detonations and the coupling with the highly state-dependent reactions. Apart from the Richtmyer–Meshkov and Kelvin–Helmholtz instabilities favouring vorticity production and mixing, much of the turbulent fluctuation is expected to be driven directly by the chemical energy release at small scales via violent volumetric expansions of the gas driving pressure waves. We hence expect a situation where the solenoidal components of the turbulent fluctuations may be as important as the dilatational components, a situation studied very little in the past. Thus, turbulence models capturing these compressible turbulence mechanisms must be developed to provide closure of the rates of mechanical, thermal and chemical relaxation rates, as given by the right-hand sides of the Favre-averaged conservation equations for momentum (A 24), energy (A 25) and reaction scalar (A 26) given in the Appendix.

6. Conclusions

The present work has analysed the reaction zone structure of both highly unstable and weakly unstable detonations and determined how the various physical phenomena observed in the reaction zone structure affect the global one-dimensional average structure of the wave. First, we find that the global behaviour of the wave and energy partition between fluctuations and mean values can be rationalized in a one-dimensional average model, suggesting the possibility of modelling complex detonation waves by a stochastic one-dimensional approach. Two important time (or length) scales were identified: the time scale of chemical energy release during which fluctuations are driven by the exothermicity and flow instabilities, and the location of the sonic surface, which appears to be delayed due to the slower rate of dissipation of hydrodynamic fluctuations, which act as a slower exothermic process. By detailed comparison between experiments and numerical simulations, and detailed investigation of the numerical limitations, we find that a correct model for the global energy release in highly unstable detonations should involve the mechanism of turbulent mixing between gases at various stages of their diffusionless oxidation process, generated by Kelvin–Helmholtz and Richtmyer–Meshkov hydrodynamic instabilities.

We wish to acknowledge the financial support of FCAR, NSERC, EPSRC, DSTL, and the BP-Ford Carbon Mitigation Initiative at Princeton University for this research. We thank Charles Kiyanda for providing one of his multiple frame photographs prior to its publication. The first author also wishes to acknowledge very useful discussions with Joe Shepherd, Joe Powers and Dave Kassoy during the preparation of the manuscript.

Appendix

Favre-averaged equations

We present here for completeness the Favre-averaged equations for the reacting compressible Navier–Stokes equations and their specialization to one-dimensional stationary flows like those encountered for detonation waves. The non-reactive version was first derived in Favre (1965). We assume that all variables of interest (pressure, density, momenta and energies) are turbulent, i.e. stochastic random variables. The averaging procedure is assumed to be a stochastic one, i.e. by taking moments of the probability distributions of the various quantities. This corresponds to taking ensemble averages of different realizations in a practical situation.

The governing equations are the reactive Navier–Stokes equations

$$\left.\begin{aligned}
&\rho_t + \nabla\cdot(\rho\boldsymbol{u}) = 0,\\
&(\rho\boldsymbol{U})_t + \nabla\cdot(\rho\boldsymbol{u}\boldsymbol{u}) + \nabla_p) = -\nabla\cdot\boldsymbol{\sigma},\\
&(\rho e)_t + \nabla\cdot((\rho e + p)\boldsymbol{u}) = -\nabla\cdot\boldsymbol{q}_T - \nabla\cdot(\boldsymbol{u}\cdot\sigma) - Q\nabla\cdot\boldsymbol{q}_D,\\
&(\rho\alpha)_t + \nabla\cdot(\rho\boldsymbol{u}\alpha) = \rho\dot{w} - \nabla\cdot\boldsymbol{q}_D,
\end{aligned}\right\} \tag{A 1}$$

where equations (3.5)–(3.8) have been augmented by the diffusive terms involving the molecular stress tensor $\boldsymbol{\sigma}$, the heat conduction flux $\boldsymbol{q}_T$, and the mass flux $\boldsymbol{q}_D$ of the reacting scalar α.

Each stochastic variable w is decomposed into a mean and fluctuating component, according to

$$w(x, y, z, t) = \bar{w}(x, y, z, t) + w'(x, y, z, t), \tag{A 2}$$

where the overbar represents stochastic averaging. Since in compressible flows each fluid element is compressed or expanded, we are not interested in the local fluid velocity $\boldsymbol{u}$ and energy contribution e, but rather in the momentum and energy density $\rho\boldsymbol{u}$ and ρe. This means that we are treating the products $\rho\boldsymbol{u}$ and ρe as stochastic variables, instead of the individual components. This is the basis of Favre-averaging, where density is used to weight the statistical averages for many fluid elements. The decomposition of the variables of interest thus becomes

$$p(x, y, z, t) = \bar{p}(x, y, z, t) + p'(x, y, z, t), \tag{A 3}$$

$$\rho\boldsymbol{u}(x, y, z, t) = \overline{\rho\boldsymbol{u}}(x, y, z, t) + (\rho\boldsymbol{u})'(x, y, z, t), \tag{A 4}$$

$$\rho e(x, y, z, t) = \overline{\rho e}(x, y, z, t) + (\rho e)'(x, y, z, t). \tag{A 5}$$

From this choice of averaging procedure, one can define (for convenience, but not necessary) a Favre-averaged velocity $\tilde{\boldsymbol{u}}$ and energy $\tilde{e}$ as

$$\overline{\rho\boldsymbol{u}} \equiv \bar{\rho}\tilde{\boldsymbol{u}}, \tag{A 6}$$

$$\overline{\rho e} \equiv \bar{\rho}\tilde{e}. \tag{A 7}$$

With these new definitions, we can also define fluctuating quantities $\boldsymbol{u}''$ and e'' as

$$\boldsymbol{u}'' \equiv \boldsymbol{u} - \tilde{\boldsymbol{u}}, \tag{A 8}$$

$$e'' \equiv e - \tilde{e} \tag{A 9}$$

such that

$$\overline{\rho\boldsymbol{u}''} = \overline{\rho e''} = 0. \tag{A 10}$$

The temperature, kinetic energy and internal energy are treated by the same formalism as the energy e. The averaged equation of state for a perfect gas is simply

$$\bar{p} = \overline{\rho R T} \equiv \bar{\rho} R \tilde{T} \tag{A 11}$$

and the averaged caloric equation of state for a perfect gas relates the internal energy e_* to the adiabatic exponent γ and the average pressure and density by

$$\overline{\rho e_*} \equiv \bar{\rho}\tilde{e}_* = \frac{\bar{p}}{\gamma - 1}. \tag{A 12}$$

Taking first-order moments of the governing equations, after some algebraic manipulations, the Favre-averaged mass and momentum equations become

$$\frac{\partial \bar{\rho}}{\partial t} + \frac{\partial}{\partial x_j}(\bar{\rho}\tilde{u}_j) = 0, \tag{A 13}$$

$$\frac{\partial(\bar{\rho}\tilde{u}_i)}{\partial t} + \frac{\partial}{\partial x_j}(\bar{\rho}\tilde{u}_i\tilde{u}_j + \bar{p}) = -\frac{\partial}{\partial x_j}\bar{\sigma}_{ij} - \frac{\partial}{\partial x_j}(\overline{\rho u_i'' u_j''}). \tag{A 14}$$

Clearly, the choice of Favre-averaging does not introduce any new terms into the mass conservation equation. The momentum equation has the familiar Reynolds stress, similar to incompressible flow, although the velocity fluctuations are weighted by the local fluid density. The energy equation for high-speed flow is best written in terms of the enthalpy h. After some manipulation, and making use of the mass and momentum conservation equations, the averaged form now becomes

$$\bar{\rho}\frac{\tilde{\mathrm{D}}\tilde{h}}{\mathrm{D}t} - \frac{\partial \bar{p}}{\partial t} = -\frac{\partial}{\partial x_j}(Q\bar{q}_{D,j} + \bar{q}_{T,j} + \tilde{u}_i\bar{\sigma}_{ij} + \overline{u_i''\sigma_{ij}}) - \frac{\partial}{\partial t}\left(\tfrac{1}{2}\overline{\rho u_i'' u_i''}\right) \\ - \frac{\partial}{\partial x_j}\left(\frac{\gamma}{\gamma-1}\overline{p' u_j''} + Q\overline{\rho\alpha'' u_i''} + \tfrac{1}{2}\tilde{u}_j\overline{\rho u_i'' u_i''} + \tilde{u}_i\overline{\rho u_i'' u_j''} + \tfrac{1}{2}\overline{\rho u_j'' u_i'' u_i''}\right) \quad \text{(A 15)}$$

where the convective derivative in the macroscopic motion is

$$\frac{\tilde{\mathrm{D}}}{\mathrm{D}t} \equiv \frac{\partial}{\partial t} + \tilde{u}_j\frac{\partial}{\partial x_j} \quad \text{(A 16)}$$

and the Favre-averaged total enthalpy is

$$\tilde{h} \equiv \tilde{e} + \frac{\bar{p}}{\bar{\rho}} = \frac{\gamma\bar{p}/\bar{\rho}}{\gamma-1} + \tfrac{1}{2}\tilde{u}_i\tilde{u}_i + \tilde{\alpha}Q. \quad \text{(A 17)}$$

There are several new terms appearing on the right-hand side of the conservation of total enthalpy (A 15). The first three are the averaged diffusive terms appearing in the non-averaged conservation. The fourth term is the non-dissipative work of molecular stresses in the velocity fluctuations. The fifth term is the unsteady change of the turbulent kinetic energy. The sixth term is the turbulent transport of enthalpy fluctuations. The seventh term is the turbulent transport of chemical energy. The remaining terms involve the changes in the turbulent kinetic energy.

Finally, the averaged conservation of species becomes

$$\frac{\partial(\bar{\rho}\tilde{\alpha})}{\partial t} + \frac{\partial}{\partial x_i}(\bar{\rho}\tilde{u}_i\tilde{\alpha}) = \bar{\dot{w}} + \frac{\partial}{\partial x_i}\overline{q_{D,i}} + \frac{\partial}{\partial x_i}\overline{\rho\alpha'' u_i''}, \quad \text{(A 18)}$$

with the extra term corresponding to the turbulent transport of species by the microscopic fluctuations (Peters 2000).

One-dimensional stationary Favre-average equations

For propagating detonation waves, we are interested in the statistical structure of the detonation in the direction of propagation only, i.e. we seek a one-dimensional probabilistic structure, treating the departure from one-dimensionality as fluctuation. We shall also assume a statistically stationary structure, i.e. a wave propagating with a constant time-averaged velocity $\bar{V}$ and characterized by a statistically similar spatial structure in the detonation wave frame of reference. The Favre equations for the stationary one-dimensional reaction zone structure can thus be further simplified with

$$\frac{\partial}{\partial t} = \frac{\partial}{\partial x_2} = \frac{\partial}{\partial x_3} = 0 \quad \text{(A 19)}$$

and

$$\tilde{u}_2 = \tilde{u}_3 = 0. \quad \text{(A 20)}$$

In the wave frame of reference, given by

$$x_1' = \bar{V}t - x_1, \quad \text{(A 21)}$$

and assuming isotropic velocity fluctuations, i.e.

$$u_1'' = u_2'' = u_3'' \equiv u'', \quad \text{(A 22)}$$

the Favre-averaged equations in the x'-direction become

$$\frac{\mathrm{d}}{\mathrm{d}x'}\left(\bar{\rho}\tilde{u}\right) = 0, \tag{A 23}$$

$$\frac{\mathrm{d}}{\mathrm{d}x'}\left(\bar{\rho}\tilde{u}^2 + \bar{p}\right) = -\frac{\mathrm{d}}{\mathrm{d}x'}\left(\bar{\sigma}_{1j} + \overline{\rho u''^2}\right) \tag{A 24}$$

$$\begin{aligned}\bar{\rho}\tilde{u}\frac{\mathrm{d}\tilde{h}}{\mathrm{d}x'} &= \frac{\mathrm{d}}{\mathrm{d}x'}\left(-Q\bar{q}_D + \bar{q}_T + \tilde{u}\bar{\sigma} + \overline{u_i''\sigma_{i1}}\right) \\ &\quad - \frac{\mathrm{d}}{\mathrm{d}x'}\left(\frac{\gamma}{\gamma-1}\overline{p'u''} + Q\overline{\rho\alpha''u''} + \frac{b+2}{2}\tilde{u}\overline{\rho u''u''} + \frac{b}{2}\overline{\rho u''u''u''}\right),\end{aligned} \tag{A 25}$$

$$\frac{\mathrm{d}}{\mathrm{d}x'}\left(\bar{\rho}\tilde{u}\tilde{\alpha}\right) = \bar{\dot{w}} + \frac{\mathrm{d}}{\mathrm{d}x'}\overline{q_D} + \frac{\mathrm{d}}{\mathrm{d}x'}\overline{\rho\alpha''u''} \tag{A 26}$$

where $b = 2$ and 3 for two-dimensional and three-dimensional problems respectively. Clearly, the only independent variable x' can be substituted by a time coordinate, corresponding to the time taken for an average Lagrangian fluid variable traversing the average reaction zone structure, by the simple substitution,

$$\mathrm{d}t = \mathrm{d}x'/\tilde{u}. \tag{A 27}$$

Hugoniot analysis

The governing equations can also be integrated once to establish the effect of the fluctuating quantities on the global properties of the wave. A similar treatment was performed by White (1962) and Rybanin (1966) for a simpler system where only the Reynolds stress in (A 24) and the seventh term on the right-hand side of (A 25) were retained to describe the structure of the solution. The solution derived here is also different, since, due to the Favre-averaging, density appears on the right-hand side of the governing equations. The equations of mass, momentum and energy can be integrated, taking the initial state as reference. Normalizing the equations with the initial density ρ_o as reference density, the ideal detonation velocity V_{CJ} as reference velocity, V_{CJ}^2 as energy scale and $\rho_o V_{CJ}^2$ as pressure scale, the integrated equations of motion become

$$\bar{\rho}\tilde{u} = \bar{V}, \tag{A 28}$$

$$\bar{\rho}\tilde{u}^2 + \bar{p} + f = \bar{V}^2 + \frac{1}{\gamma M_{CJ}^2}, \tag{A 29}$$

$$\frac{\gamma}{\gamma-1}\frac{\bar{p}}{\bar{\rho}} + \tilde{\alpha}Q + \tfrac{1}{2}\tilde{u}^2 + \frac{g}{\bar{V}} = \frac{1}{M_{CJ}^2(\gamma-1)} + Q + \tfrac{1}{2}\bar{V}^2, \tag{A 30}$$

where M_{CJ} is the ideal detonation Mach number. In this new notation the unknown detonation velocity $\bar{V}$ is thus normalized by the ideal CJ velocity. Since this is unknown, it appears in the source term of the energy equation as $g/\bar{V}$, where g represents the energy sources in (A 25), i.e.

$$g \equiv Q\bar{q}_D + \bar{q}_T + \tilde{u}\bar{\sigma} + \overline{u_i''\sigma_{i1}} + \frac{\gamma}{\gamma-1}\overline{p'u''} + Q\overline{\rho\alpha''u''} + \frac{b+2}{2}\tilde{u}\overline{\rho u''^2} + \frac{b}{2}\overline{\rho u''^3}. \tag{A 31}$$

The presence of this term involving the unknown detonation velocity is a departure from the treatment of White (1962) and Rybanin (1966), due to the Favre averaging as opposed to conventional averaging in incompressible flows. Likewise, f is the source term in the momentum equation

$$f \equiv \bar{\sigma}_{1j} + \overline{\rho u''^2}. \tag{A 32}$$

The Hugoniot equation is obtained by combining the energy and momentum equations. After some manipulation, we obtain the relationship between pressure and specific volume $(1/\rho)$ as

$$\bar{p} = \frac{\dfrac{1}{\gamma M_{CJ}^2}\left(\dfrac{\gamma+1}{\gamma-1} - \dfrac{1}{\bar{\rho}}\right) + 2(1-\tilde{\alpha})\,Q + f\left(\dfrac{1}{\bar{\rho}} + 1\right) - 2\dfrac{g}{\bar{V}}}{\dfrac{\gamma+1}{\gamma-1}\dfrac{1}{\bar{\rho}} - 1}. \tag{A 33}$$

In the absence of the source terms f and g, the above expression is simply the partial reaction Hugoniot (Fickett & Davis 1979). The presence of the energy sources g and f has the tendency to shift the pressure either up or down depending on the magnitude and sign of the various terms.

The Rayleigh line, describing the conservation of momentum and mass, can also be derived as

$$\bar{p} = \frac{1}{\gamma M_{CJ}^2} + \bar{V}^2\left(\frac{\gamma+1}{\gamma-1} - \frac{1}{\bar{\rho}}\right) - f. \tag{A 34}$$

The departure of the Rayleigh line from the ideal straight line comes from the mechanical fluctuation f. The behaviour of the viscous stress and Reynolds stress is opposite in the reaction zone. Since Reynolds stress is a positive quantity, the real Rayleigh line lies below the ideal one in the (p, ρ^{-1})-plane. However, the one-dimensional viscous stress has the opposite sign in the region of positive velocity gradient, when the gases are accelerated by the energy deposition. In general, we expect the turbulent fluctuations to play a more important role.

REFERENCES

Arienti, M. & Shepherd, J. E. 2005 The role of diffusion in irregular detonations. *The 4th Joint Meeting of the US Sections of the Combustion Institute, Philadelphia, PA, March 20–23.*

Austin, J. 2003 The role of instability in gaseous detonation. PhD thesis, California Institute of Technology, Pasadena, California.

Austin, J. M., Pintgen, F. & Shepherd, J. E. 2005 Reaction zones in highly unstable detonations. *Proc. Combust. Inst.* **30**, 1849–1857.

Bourlioux, A. & Majda, A. J. 1992 Theoretical and numerical structure for unstable two dimensional detonations. *Combust. Flame* **90**, 211–229.

Deiterding, R. 2003 Parallel adaptive simulation of multi-dimensional detonation structures. PhD thesis, Brandenburgischen Technischen Universität Cottbus.

Deledicque, V. & Papalexandris, M. V. 2006 Computational study of three-dimensional gaseous detonation structures. *Combust. Flame* **144**, 821–837.

Edwards, D. H., Hooper, G., Job, E. M. & Parry, D. J. 1970 The behavior of the frontal and transverse shocks in gaseous detonation waves. *Astronaut. Acta* **15**, 323–333.

Edwards, D. H., Jones, A. J. & Phillips, D. E. 1976 Location of Chapman – Jouguet surface in a multiheaded detonation-wave. *J. Phys. D* **9**, 1331–1342.

Edwards, D. H., Jones, T. G. & Price, B. 1963 Observations on oblique shock waves in gaseous detonations. *J. Fluid Mech.* **17**, 21–34.

Eto, K., Tsuboi, N. & Hayashi, A. K. 2005 Numerical study on three-dimensional C-J detonation waves: detailed propagating mechanism and existence of OH radical. *Proc. Combust. Inst.* **30**, 1907–1913.

Falle, S. A. E. G. 1991 Self-similar jets. *Mon. Not. R. Astron. Soc.* **250**, 581–596.

Falle, S. A. E. G. & Giddings, J. R. 1993 Body capturing. In *Numerical Methods for Fluid Dynamics* (ed. K. W. Morton & M. J. Baines), vol. 4, pp. 337–343. Clarendon.

Falle, S. A. E. G. & Komissarov, S. S. 1996 An upwind scheme for relativistic hydrodynamics with a general equation of state. *Mon. Not. R. Astron. Soc.* **278**, 586–602.

Favre, A. 1965 Equations des gas turbulents compressibles. *J. Méc.* **4**, 361–421.

FICKETT, W. & DAVIS, W. C. 1979 *Detonation.* University of California Press.

FRISCH, U. 1995 *Turbulence.* Cambridge University Press.

GAMEZO, V. N., DESBORDES, D. & ORAN, E. S. 1999 Formation and evolution of two-dimensional cellular detonations. *Combust. Flame* **116**, 154–165.

GORDON, S. & MCBRIDE, B. J. 1994 Computer program for calculation of complex chemical equilibrium compositions and applications. *NASA RP*-1311.

HENRICK, A. K., ASLAM, T. D. & POWERS, J. M. 2006 Simulations of pulsating one-dimensional detonations with true fifth order accuracy. *J. Comput. Phys.* **213**, 311–329.

HU, X. Y., ZHANG, D. L., KHOO, B. C. & JIANG, Z. L. 2005 The structure and evolution of a two-dimensional H-2/O-2/Ar cellular detonation. *Shock Waves* **14**, 37–44.

INABA, K., MATSUO, A. & TANAKA, K. 2005 Numerical investigation on acoustic coupling of transverse waves in two-dimensional H-2-O-2-diluent detonations. *Trans. Japan Soc. Aero. Space Sci.* **47** (158), 249–255.

KASIMOV, A. R. & STEWART, D. S. 2004 On the dynamics of self-sustained one-dimensional detonations: a numerical study in the shock-attached frame. *Phys. Fluids* **16**, 3566–3578.

KHOKHLOV, A. M., ORAN, E. S. & THOMAS, G. O. 1999 Numerical simulation of deflagration-to-detonation transition: the role of shock–flame interactions in turbulent flames. *Combust. Flame* **117**, 323–339.

KISTIAKOWSKY, G. B. & KYDD, P. H. 1956 Gaseous detonations. IX. A study of the reaction zone by gas density measurements. *J. Chem. Phys.* **25**, 824–835.

KIYANDA, C. B. 2005 Photographic study of the structure of irregular detonation waves. Master's thesis, McGill University, Montreal, Canada.

KIYANDA, C. B., HIGGINS, A. J. &. LEE, J. H. S. 2005 Photographic study of the two-Dimensional dynamics of irregular detonation waves. Paper presented at the 20th *Intl Colloquium on the Dynamics of Explosions and Reactive Systems, Montreal, Canada, July 31–August 5* (on CD-ROM).

LABERGE, S., KNYSTAUTAS, R. & LEE, J. H. S. 1993 Propagation and extinction of detonation waves in tube bundles. *Prog. Astro. Aero.* **153**, 381–396.

LEE, J. H. 1984 Dynamic parameters of gaseous detonations. *Annu. Rev. Fluid. Mech.* **16**, 311–336.

LEE, J. H. S. & RADULESCU, M. I. 2005 On the hydrodynamic thickness of cellular detonations. *Fizika Goreniya i Vzryva*, **41**(6), 157–180 (in Russian), translated in *Combust. Explo. Shock Waves* **41**(6), 745–765.

LUTZ, A. E., KEE, R. J., MILLER, J. A., DWYER, H. A. & OPPENHEIM, A. K. 1988 Dynamic effects of autoignition centers for hydrogen and C1,2-hydrocarbon fuels. *Proc. Combust. Inst.* **22**, 1683–1693.

MANZHALEI, V. I. 1977 Fine structure of the leading front of a gas detonation. *Fizika Goreniya I Vzryva* **13**, 470–472 (in Russian). Translated in *Combust. Explo. Shock Waves* **13**(3), 402–404.

NG, H. D., HIGGINS, A. J., KIYANDA, C. B., RADULESCU, M. I., LEE, J. H. S., BATES, K. R. & NIKIFORAKIS, N. 2005*a* Nonlinear dynamics and chaos analysis of one-dimensional pulsating detonations. *Combust. Theory Modell.* **9**, 159–170.

NG, H. D., RADULESCU, M. I., HIGGINS, A. J., NIKIFORAKIS, N. & LEE, J. H. S. 2005*b* Numerical investigation of the instability for one-dimensional Chapman-Jouguet detonations with chain-branching kinetics. *Combust. Theory Modell.* **9**, 385–401.

NIKOLAEV, YU. A. & ZAK, D. V. 1989 Quasi-one-dimensional model of self-sustaining multifront gas detonation with losses and turbulence taken into account. *Combust. Explo. Shock Waves* **25**, 103–112.

ORAN, E. S., WEBER, J. W., STEFANIW, E. I., LEFEBVRE, M. H. & ANDERSON, J. D. 1998 A numerical study of a two-dimensional H-2-O-2-Ar detonation using a detailed chemical reaction model. *Combust. Flame* **113**, 147–163.

ORAN, E. S., YOUNG, T. R., BORIS, J. P., PICONE, J. M. & EDWARDS, D. H. 1982 A study of detonation structure: the formation of unreacted pockets. In *Nineteenth Symp. (Intl) on Combustion*, pp. 573–582. Pittsburgh: the Combustion Institute.

PANTON, R. 1971 Effects of structure on average properties of two-dimensional detonations. *Combust. Flame* **16**, 75–82.

PETERS, N. 2000 *Turbulent Combustion.* Cambridge University Press.

PINTGEN, F., ECKETT, C. A., AUSTIN, J. M. & SHEPHERD, J. E. 2003 Direct observations of reaction zone structure in propagating detonations. *Combust. Flame* **133**, 211–229.

Quirk, J. J. 1994 Godunov-type schemes applied to detonation flows. In *Combustion in High Speed Flows* (ed. J. Buckmaster, T. L. Jackson & A. Kumar), pp. 575–596. Kluwer.

Radulescu, M. I. 2003 The propagation and failure mechanism of gaseous detonations: experiments in porous-walled tubes. PhD thesis, McGill University, Montreal, Canada.

Radulescu, M. I. & Lee, J. H. S. 2002 The failure mechanism of gaseous detonations: experiments in porous wall tubes. *Combust. Flame* **131**, 29–46.

Radulescu, M. I., Sharpe, G. J., Lee, J. H. S., Kiyanda, C., Higgins, A. J. & Hanson, R. K. 2005 The ignition mechanism in irregular structure gaseous detonations. *Proc. Combust. Inst.* **30**, 1859–1867.

Rybanin, S. S. 1966 Turbulence in detonations. *Combust. Explo. Shock Waves* **2**, 29–35.

Sharpe, G. J. 2001 Transverse waves in numerical simulations of cellular detonations. *J. Fluid Mech.* **447**, 31–51.

Sharpe, G. J. & Falle, S. A. E. G. 2000. Two-dimensional numerical simulations of idealized detonations. *Proc. R. Soc. Lond.* A **456**, 2081–2100.

Shepherd, J. E. 1986 Chemical kinetics of hydrogen-air-diluent mixtures. *Prog. Astro. Aero.* **106**, 263–293.

Soloukhin, R. I. 1966 Multiheaded structure of gaseous detonation. *Combust. Flame* **10**, 51–58.

Strehlow, R. A. 1971 Detonation structure and gross properties. *Combust. Sci. Tech.* **4**, 65–71.

Subbotin, V. 1975*a* Two kinds of transverse wave structures in multi-front detonation. *Combust. Explo. Shock Waves* **11**, 96–102.

Subbotin, V. 1975*b* Collision of transverse detonation waves in gases. *Combust. Explo. Shock Waves* **11**, 411–414.

Svehla, R. A. 1995 Transport coefficients for the NASA chemical equilibrium program. *NASA TM* 4647.

Taylor, G. I. 1950 The dynamics of the combustion products behind plane and spherical detonation fronts in explosives. *Proc. R. Soc. Lond.* A **200**, 235–247.

Thomas, G. O. & Edwards, D. H. 1983 Simulation of detonation cell kinematics using two-dimensional reactive blast waves. *J . Phys. D* **16**, 1881–1892.

Voitsekhovskii, B. V., Mitrofanov, V. V. & Topchian, M. E. 1963 Structure of a detonation front in gases. *Izd. Akad. Nauk SSSR, Novosibirsk.*

White, D. R. 1961 Turbulent structure of gaseous detonation. *Phys. Fluids* **4**, 465–480.

Williams, F. A. 1985 *Combustion Theory*, 2nd Edn. Perseus Books Publishing.